SANDIA REPORT

SAND2007-0422
Unlimited Release
Printed January 2007

Analytic and Computational Micromechanics of Clustering and Interphase Effects in Carbon Nanotube Composites

Gary D. Seidel, Daniel C. Hammerand, Dimitris C. Lagoudas

Prepared by
Sandia National Laboratories
Albuquerque, New Mexico 87185 and Livermore, California 94550

Sandia is a multiprogram laboratory operated by Sandia Corporation,
a Lockheed Martin Company, for the United States Department of Energy's
National Nuclear Security Administration under Contract DE-AC04-94-AL85000.

Issued by Sandia National Laboratories, operated for the United States Department of Energy by Sandia Corporation.

Available to DOE and DOE contractors from
U.S. Department of Energy
Office of Scientific and Technical Information
P.O. Box 62
Oak Ridge, TN 37831

Telephone: (865) 576-8401
Facsimile: (865) 576-5728
E-Mail: reports@adonis.osti.gov
Online ordering: http://www.osti.gov/bridge

Available to the public from
U.S. Department of Commerce
National Technical Information Service
5285 Port Royal Rd
Springfield, VA 22161

Telephone: (800) 553-6847
Facsimile: (703) 605-6900
E-Mail: orders@ntis.fedworld.gov
Online ordering: http://www.ntis.gov/help/ordermethods.asp?loc=7-4-0#online

SAND2007-0422
Unlimited Release
Printed January 2007

Analytic and Computational Micromechanics of Clustering and Interphase Effects in Carbon Nanotube Composites

Gary D. Seidel
Sandia National Laboratories/Texas A&M University
Doctoral Fellowship in Engineering Recipient
Texas A&M University
College Station, TX 77843-3141
gary-don@tamu.edu

Daniel C. Hammerand
Sandia National Laboratories
P.O. Box 5800
MS 0893
Albuquerque, NM 87185-0893
dchamme@sandia.gov

Dimitris C. Lagoudas
John and Bea Slattery Chair of Aerospace Engineering
Aerospace Engineering Department
Texas A&M University
College Station, TX 77843-3141
dlagoudas@aero.tamu.edu

Abstract

Effective elastic properties for carbon nanotube reinforced composites are obtained through a variety of micromechanics techniques. Using the in-plane elastic properties of graphene, the effective properties of carbon nanotubes are calculated utilizing a composite cylinders micromechanics technique as a first step in a two-step process. These effective properties are then used in the self-consistent and Mori-Tanaka methods to obtain effective elastic properties of composites consisting of aligned single or multi-walled carbon nanotubes embedded in a polymer matrix. Effective composite properties from these averaging methods are compared to a direct composite cylinders approach extended from the work of Hashin and Rosen (1964) and Christensen and Lo (1979). Comparisons with finite element simulations are also performed. The effects of an interphase layer between the nanotubes and the polymer matrix as result of functionalization is also investigated using a multi-layer composite cylinders approach. Finally, the modeling of the clustering of nanotubes into bundles due to interatomic forces is accomplished herein using a tessellation method in conjunction with a multi-phase Mori-Tanaka technique. In addition to aligned nanotube composites, modeling of the effective elastic properties of randomly dispersed nanotubes into a matrix is performed using the Mori-Tanaka method, and comparisons with experimental data are made.

Computational micromechanical analysis of high-stiffness hollow fiber nanocomposites is performed using the finite element method. The high-stiffness hollow fibers are modeled either directly as isotropic hollow tubes or equivalent transversely isotropic effective solid cylinders with properties computed using a micromechanics based composite cylinders method. Using a representative volume element for clustered high-stiffness hollow fibers embedded in a compliant matrix with the appropriate periodic boundary conditions, the effective elastic properties are obtained from the finite element results. These effective elastic properties are compared to approximate analytical results found using micromechanics methods. The effects of an interphase layer between the high-stiffness hollow fibers and matrix to simulate imperfect load transfer and/or functionalization of the hollow fibers is also investigated and compared to a multi-layer composite cylinders approach. Finally the combined effects of clustering with fiber-matrix interphase regions are studied. The parametric studies performed herein were motivated by and used properties for single-walled carbon nanotubes embedded in an epoxy matrix, and as such are intended to serve as a guide for continuum level representations of such nanocomposites in a multi-scale modeling approach.

Acknowledgment

The authors graciously acknowledge the support provided by Sandia National Laboratories, a multiprogram laboratory operated by Sandia Corporation, a Lockheed Martin Company, for the U.S. Department of Energy under Contract DE-AC04-94AL85000, and in addition, the support provided by the Texas Institute for Intelligent Bio-Nano Materials and Structures for Aerospace Vehicles, funded by NASA Cooperative Agreement No. NCC-1-02038. Any opinions, findings, and conclusions or recommendations expressed in this material are those of the author(s) and do not necessarily reflect the views of the National Aeronautics and Space Administration. Finally, the authors would like to thank Mr. Piyush Thakre for providing the images used in Figure 1.1 with material produced in the laboratory of Dr. Rick Barrera at Rice University.

Contents

Appendix

List of Figures

List of Tables

Preface

This document is prepared as a final deliverable for an LDRD Fellowship program conducted between Sandia National Laboratories and Texas A&M University. The work presented here is taken from two journal articles accepted for publication during the course of the fellowship; Seidel and Lagoudas (2006a) and Hammerand et al. (2007).

Chapter 1

Introduction

Since the discovery of carbon nanotubes (CNTs) by Iijima (1991), CNTs have become a subject of much research across a multitude of disciplines. A single-walled carbon nanotube (SWCNT) can be viewed as a single sheet of graphite (i.e. graphene), which has been rolled into the shape of a tube (Saito et al., 1998). SWCNTs have radii on the order of nanometers and lengths on the order of micrometers resulting in large aspect ratios beneficial to their use in composites. (Saito et al., 1998; Roche, 2000). Carbon nanotubes can be either metallic or semi-conducting depending on the tubes chiral, or roll-up angle, which indicates the orientation of the hexagonal carbon rings relative to the tube axis (Roche, 2000; Saito et al., 1998). However, it is the mechanical properties of carbon nanotubes as they pertain to their use in composites that are of interest herein. Carbon nanotubes are reported to have an axial Young's modulus in the range of 300-1000 GPa, up to five times the stiffness and with half the density of SiC fibers, in addition to having a theoretically predicted elongation to break of 30-40% (Yakobson and Smalley, 1997; Salvetat-Delmotte and Rubio, 2002; Yu et al., 2000a; Yakobson et al., 1997; Wang et al., 2001; Fisher, 2002; Popov, 2004).

A wide variety of composites containing CNTs have been manufactured. Peigney et al. (2000) have fabricated composites specimens of CNTs embedded in ceramic powders while Milo et al. (1999) have embedded CNTs in poly(vinyl alcohol). Meltmixing has been used by Potschke et al. (2004) to introduce CNTs into a polyethylene matrix. Such efforts have identified several key challenges in the fabrication of CNT composites. Adequate dispersion of CNTs within the matrix has been a key issue given the tendency of CNTs to form bundles due to interatomic forces (Gong et al., 2000; Zhu et al., 2003). Adhesion of the CNTs to the surrounding matrix has been another key issue (Star et al., 2001) as has orientation of CNTs and bundles of CNTs within the matrix (Jin et al., 1998). Efforts to address the adhesion and dispersion issues in particular have lead to the use of polymer-wrapped CNTs and functionalized CNTs producing distinct interphase regions between matrix and CNTs (Star et al., 2001; Zhu et al., 2003; McCarthy et al., 2002; in het Panhuis et al., 2003; Wagner et al., 1998; Lourie and Wagner, 1998).

Experimental measurement of the effective properties of CNT reinforced polymer matrix composites have indicated substantial increases in the composite modulus over the matrix modulus. Schadler et al. (1998) found a 40% increase in the effective stiffness of CNT reinforced epoxy as compared to the matrix value with 5% weight CNTs. Qian et al.

(2000) also found an increase in the effective modulus of CNT reinforced polystyrene to be on the order of 40% for just 1% weight CNTs. The stress-strain response of functionalized CNTs in epoxy has been observed by Zhu et al. (2004) and found to yield an increase in the effective properties on the order of 30% to 70% at weight percents of 1% and 4% CNTs.

Modeling of composites containing CNTs has also received attention in recent years. Frankland et al. (2002) have used molecular dynamics (MD) to obtain the stress-strain behavior of CNTs embedded in a polymer matrix. Liu and Chen (2003) studied the mechanical response in tension of a single CNT embedded in polymer via finite element analysis. In a series of papers, Odegard et al. (2003), Odegard and Gates (2002), Odegard et al. (2002a), Odegard et al. (2002b), and Odegard et al. (2001) have modeled CNT composites using the equivalent continuum method in conjunction with the Mori-Tanaka micromechanics method to obtain the effective elastic constants for both aligned and misaligned CNTs and found effective elastic moduli to be several times that of the matrix for aligned CNTs and almost one and half time the matrix value for misaligned CNTs at a volume fraction of 1% CNTs. Experimentally obtained values for effective Young's modulus being substantially lower, other research efforts have sought to include additional aspects of CNT composites in the calculation of effective properties. For example, the effects of nanotube waviness on the effective composite properties have been studied by Fisher (2002), Fisher et al. (2002), and Fisher et al. (2003) using finite element analysis in conjunction with the Mori-Tanaka method and found to lower the effective modulus. Buckling of CNTs within an epoxy matrix has been considered by Hadjiev et al. (2006). Other efforts have focused on the inclusion of less than ideal CNT adhesion to the matrix in CNT composite modeling (Wagner, 2002; Frankland et al., 2000, 2003; Griebel and Hamaekers, 2004). Herein an additional effect, the clustering of CNTs in the polymer matrix, will be considered.

In the present work, Mori-Tanaka, self-consistent, and composite cylinders analytic micromechanics approaches and finite element based computation micromechanics approaches are employed in modeling the effective elastic properties of CNT reinforced composites such as the one seen in Figure 1.1. In the largest scale image in Figure 1.1 clusters of CNTs can be seen dispersed throughout a polymer matrix. Subsequent images at smaller scales show that within each cluster, bundles of CNTs are observed to have a high degree of alignment. As such, clustering of CNTs in a polymer matrix is modeled herein in the context of aligned CNT bundles using a tessellation procedure to quantify clustering and a multi-phase Mori-Tanaka method. In addition to clustering, the effects of interphase regions due to functionalization and polymer wrapping on the effective elastic properties are also investigated using a multi-layer composite cylinders approach.

These two distinct characteristics of CNT composites, i.e., clustering of CNTs and the presence of interphase regions have recently been modeled using micromechanics methods in Seidel and Lagoudas (2006a). In the present work, the independent and combined effects of interphase regions and clustering of high-stiffness hollow fiber composites are studied using *computational* micromechanics techniques in the form of continuum finite element analysis (FEA). Finite element results are then compared to the corresponding results obtained by analytic micromechanics methods in Seidel and Lagoudas (2006a). Material

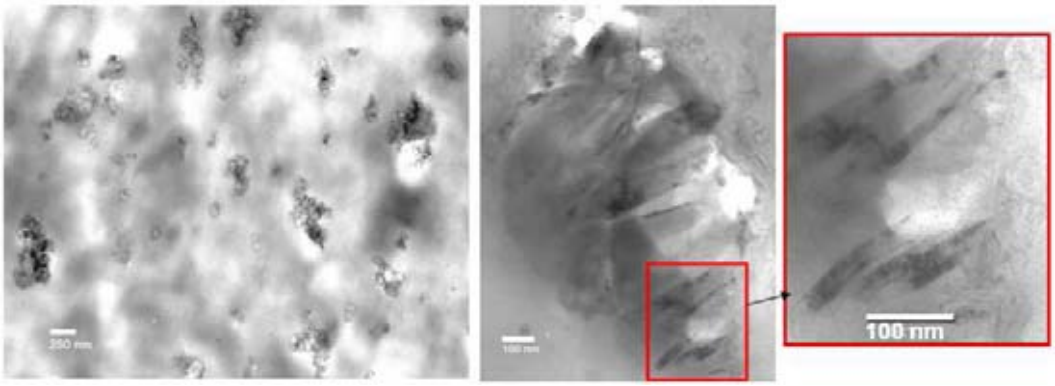

Figure 1.1. TEM images depicting clustering and alignment of CNT bundles in a polymer matrix taken using a JEOL 1200 EX TEM operating at an accelerating voltage of 100kV at Texas A&M University.

properties and geometry are taken to be reflective of continuum representations of CNT reinforced polymer-matrix (PMC) composites.

Chapter 2

Analytic Approaches to Modeling the Effective Elastic Properties of CNT Composites

For modeling purposes, the composite in Figure 1.1 has been idealized as shown in Figure 2.1(a) to a composite containing randomly oriented aligned clustered bundles of straight high aspect ratio CNTs. Effective elastic properties can be derived by first determining the effective properties of the clustered bundles as represented by the representative volume element (RVE) shown in Figure 2.1(b). In Figure 2.1(b), individual CNTs within the bundle can be seen with varying types and number of interphase regions. The effective properties of each individual CNT surrounded by its interphase regions will be determined using a multi-layer composite cylinders approach for arrangements like the one shown in Figure 2.1(c). Each unique effective CNT having differing effective properties constitutes a separate phase to be used in a multi-phase Mori-Tanaka or self-consistent approach applied to the clustered bundle of Figure 2.1(b). Finally, effective elastic properties for the composite as whole can be obtained again from a multi-phase micromechanics approach where each orientation of every distinct effective bundle constitutes a separate phase. As a first approach to modeling the effective elastic properties of the RVE shown in Figure 2.1(b), CNTs not including interphase effects will be modeled using the classical Mori-Tanaka and self-consistent techniques. A second approach using a composite cylinders model will capture the influence of interphase regions surrounding the CNTs. Efforts to include the effects of clustering within the bundles of Figure 2.1(b) will make use of both the multi-phase Mori-Tanaka and multi-layer composite cylinders techniques. The effects of random orientation will also be addressed using the Mori-Tanaka approach for a simplified version of the RVE in Figure 2.1(a) where CNTs are not clustered into bundles.

Modeling of CNT reinforced composites will proceed herein under the assumptions that the CNTs contain no defects or residual catalyst and that CNTs are straight. It has also been assumed that the CNTs are sufficiently long (having aspect ratios on the order of 1000) so as to ignore end effects. All materials, matrix, CNTs, and any interphase region, are assumed to be isotropic linear elastic, subject to small deformations. All boundaries between materials are assumed to have continuous displacements and tractions.

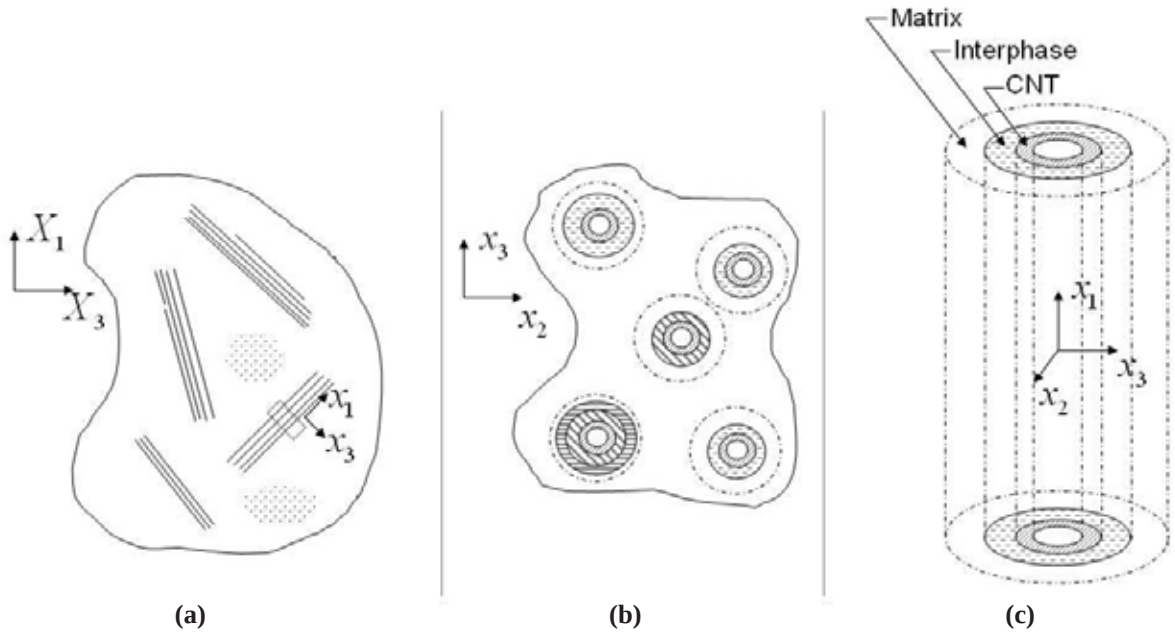

Figure 2.1. Schematic representation of clustered aligned nanotubes with interphase regions in bundles within a composite. (a) Composite level depecting aligned bundles. (b) RVE of an aligned bundle with M distinct CNT-interphase arrangements (here M=4 as two CNTs are identical). (c) Composite Cylinder assemblage for CNT with an interphase region (i.e. N=3 for the CC method and N=2 for the CC/MT or CC/SC methods)

Mori-Tanaka and Self-Consistent Averaging Methods for CNT Composites

Description of Self-Consistent and Mori-Tanaka Methods

The second step of the two step process used to obtain the effective properties of CNT reinforced composites as employed herein to model clustered bundles makes use of either the Mori-Tanaka (Mori and Tanaka, 1973; Mori et al., 1973; Weng, 1984; Benveniste, 1987) or the self-consistent methods (Hill, 1965; Budiansky, 1965). Effective CNTs obtained from a mulit-layer composite cylinders approach (referred to hereafter as CC) as discussed in Section 2 replace the CNTs and any surrounding interphases shown in Figure 2.1(b). This is done so as to be able to take advantage of the Eshelby solution (Eshelby, 1957, 1959) in the application of the Mori-Tanaka or generalized self-consistent techniques. As such, the two-step process is thus termed the CC/MT or CC/SC method, respectively. Each difference in interphase thickness or stiffness constitutes a separate phase up to P phases in the multi-phase Mori-Tanaka or self-consistent approaches.

For the CC/SC method, the effective stiffness tensor is obtained by embedding a solid cylinder having the effective CNT properties in the unknown effective composite and:

$$\mathbf{L} = \mathbf{L}_m + \sum_{l=1}^{P} c_l \left(\mathbf{L}_l - \mathbf{L}_m\right) \mathbf{A}_l \tag{2.1}$$

where

$$\mathbf{A}_l = \left[\mathbf{I} + \mathbf{S}_l \mathbf{L}^{-1} \left(\mathbf{L}_l - \mathbf{L}\right)\right]^{-1} \tag{2.2}$$

and where the bold face indicates tensor valued quantities (Lagoudas et al., 1991). In Eqns. 2.1 and 2.2, $\mathbf{L}$ is the unknown desired effective stiffness, $\mathbf{L}_m$ is the stiffness tensor of the polymer matrix, and $\mathbf{I}$ is the fourth order identity tensor. The sum over l indicates the inclusion of P separate phases the effective properties of which, $\mathbf{L}_l$, are obtained from the multi-layer composite cylinder results. The volume fraction of each separate phase is given by c_l, and $\mathbf{A}_l$ is the strain concentration factor relating the average strain in each effective cylinder to that of the unknown effective material in which it is embedded. The $\mathbf{S}_l$ in Eqn. 2.2 is the Eshelby tensor for cylindrical inclusions embedded in the unknown effective composite (i.e. for an inclusion whose shape is a cylinder and which is surrounded by a transversely isotropic material). For cases with identical CNTs with identical interphase regions or the lack thereof, P is equal to one so that c_1 is the volume fraction of effective CNTs in the polymer matrix and $\mathbf{L}_1$ is the stiffness tensor of the effective CNT as determined by relating the engineering moduli obtained from the CC method to the stiffness components. The effective stiffness tensor is thus obtained by iteratively solving Eqn. 2.1 and can then be inverted to obtain the compliance tensor, $\mathbf{M}$, from which the individual effective engineering moduli can be identified.

The same approach of using the effective CNTs as input, can be applied in using the Mori-Tanaka method resulting in the CC/MT method. The effective stiffness tensor in the CC/MT is thus obtained as:

$$\mathbf{L} = \left(c_m \mathbf{L}_m \widetilde{\mathbf{A}}_m + \sum_{l=1}^{P} c_l \mathbf{L}_l \widetilde{\mathbf{A}}_l\right) \left(c_m \mathbf{I} + \sum_{p=1}^{P} c_p \widetilde{\mathbf{A}}_p\right)^{-1} \tag{2.3}$$

where $\widetilde{\mathbf{A}}_l$ is given by:

$$\widetilde{\mathbf{A}}_l = \left[\mathbf{I} + \mathbf{S}_l \mathbf{L}_m^{-1} \left(\mathbf{L}_l - \mathbf{L}_m\right)\right]^{-1} \tag{2.4}$$

where $\widetilde{\mathbf{A}}_l$ is the concentration factor relating the average strain in the effective cylinder to the average strain of the matrix perturbed by some amount to account for interactions between inclusions. As such, the Eshelby tensor, $\mathbf{S}_l$, is obtained for cylindrical inclusions embedded in the matrix (i.e. for an inclusion whose shape is a cylinder and which is surrounded by an isotropic material), and the matrix concentration factor, $\widetilde{\mathbf{A}}_m$, as given by Eqn. 2.4 which evaluates to be the identity tensor. Further details discussing the Mori-Tanaka and self-consistent methods can be found in Lagoudas et al. (1991).

Effective Elastic Properties of Carbon Nanotubes

The first step of the CC/MT or CC/SC methods is to obtain the effective elastic constants of effective CNTs which are presumed to be transversely isotropic, i.e the $\mathbf{L}_l$ in Eqns. 2.1 through 2.4. The composite cylinders assemblage as developed by Hashin and Rosen (1964) and extended to include multiple interphase layers herein is used to obtain four out of the five independent material constants, E_{11}, ν_{12}, κ_{23}, and μ_{12}, where the subscripts are consistent with axes in Figures 2.1(c) and E, ν, κ, and μ correspond to Young's modulus, Poisson's ration, bulk modulus and shear modulus, respectively. For the fifth property, μ_{23}, the generalized self-consistent method developed by Christensen and Lo (1979) and also extended to include multiple layers is used. This combined technique as outlined in Appendix A for a general multi-layered hollow composite cylinder and is referred to herein as the CC method. Note that a sixth property, the transverse stiffness, E_{22}, is determined from the five independent effective properties from:

$$E_{22} = \frac{4\mu_{23}\kappa_{23}}{\kappa_{23} + \mu_{23} + 4\nu_{12}^2\mu_{23}\kappa_{23}/E_{11}} \tag{2.5}$$

In obtaining the effective properties of CNTs the CC method, as described in Appendix A, is applied with the number of layers, N, set equal to one so that the effective properties obtained correspond to the hollow CNT with no surrounding interphases or matrix. The CNT is presumed to have isotropic properties corresponding to those of graphite in the plane of a graphene sheet, i.e. a Young's of 1100 GPa and Poisson's ratio of 0.14 (Saito et al., 1998). This assumption is reasonable given the relative similarity between graphene sheets and nanotubes. However, material properties for nanotubes obtained from a wide variety of lower length scale calculations ranging from quantum mechanics to molecular dynamics could readily be substituted in place of graphene (Saito et al., 1998).

It should be noted that in order to apply the CC method, the inner and outer radii of the CNT must be defined, thereby introducing the thickness of the CNT as a length scale in the formulation. In single-walled CNTs, the outer radius is discernible using electron microscopy, however, estimates of the thickness of a single-walled CNT are a subject of much debate. In order to proceed with calculation of the effective properties of a single-wall carbon nanotube, geometric data indicated by Yu et al. (2000a), Ruoff and Lorents (1995), Qian et al. (2003), and Yu et al. (2000b) was employed; namely, an outer radius of 0.85nm and a thickness of 0.34nm (the interlayer spacing of graphite). Thus the volume fraction of the hollow region of the nanotube is given by $c_h = r_0^2/r_1^2$, where r_0 is the inner radius of the CNT and r_1 the outer, and is determined to have a value of $c_h = 0.36$.

CC method results for axial and transverse elastic moduli of the effective single-wall CNT are provided in Figure 2.2. In addition, results for multi-walled CNTs up to ten walls are included where, as a first approximation, it has been assumed that each additional CNT ring is perfectly bonded to neighboring CNT rings. The results in Figure 2.2 indicate that for a single-wall carbon nanotube, the difference between axial and transverse stiffness is significant, but that as one approaches a value on the order of ten rings, i.e. as the

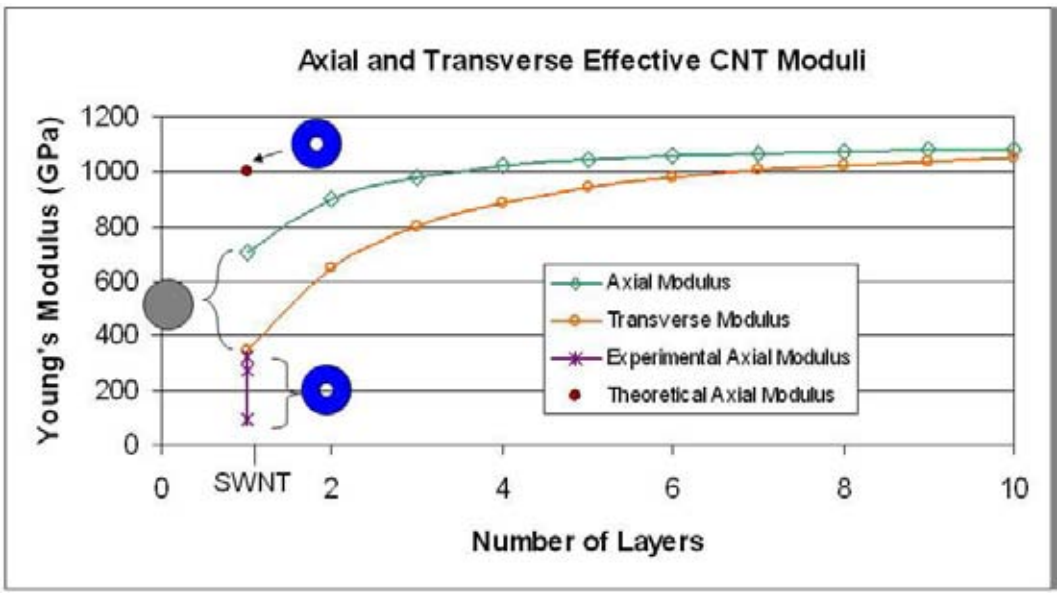

Figure 2.2. Effective CNT axial and transverse moduli obtained via the CC method with N=1 (i.e. just the CNT with no interphase) for use in the CC/MT or CC/SC methods.

volume fraction of the zero-stiffness region decreases rapidly, one approaches a nearly isotropic effective multi-walled nanotube. Also provided in Figure 2.2 are experimental results from Yu et al. (2000a) and theoretical predictions obtained by Lu (1997) for the axial stiffness of the carbon nanotube ring which demonstrate the wide range of available input data for the CC model. The hollow circles and solid circle are to remind the reader that the hollow circles correspond to actual nanotube axial moduli obtained by Lu (1997) and Yu et al. (2000a) whereas the solid circle corresponds to effective properties for the effective nanotube as calculated via the CC method. The value reported by Lu (1997) is close to the graphene modulus used to obtain the CC result. As such, using that value for the nanotube elastic modulus would produce quite similar CC results as were obtained using graphene. However, the effective nanotube stiffness obtained using the Yu et al. (2000a) data would be drastically different from those presently obtained.

It should be noted that the CC method described in Appendix A was developed for fibers embedded in a matrix, i.e. for two layers, (N=2), where the first layer is the CNT and the second is the surrounding matrix. Results for (N=1), are analogous to the results that would be obtained for a graphene sheet with cylindrical voids. Additional micromechanics techniques and finite element simulations discussed below will indicate that the effective properties obtained for CNTs via the CC method can be used to obtain reasonable results.

Composite Cylinders Model for Effective Elastic Properties of CNT Composites

Composite Cylinders Model for CNTs in the Absence of an Interphase Region

A second approach which does not treat the CNTs as effective solid cylinders, can be used to directly obtain effective composite properties for aligned carbon nanotube reinforced composites is the multi-layer composites cylinders approach. In the absence of interphase regions, the effective properties are obtained as discussed in Appendix A with the number layers equal to two as indicated in the schematic of Figure A.1 with the first layer corresponding to the CNT and the second to the matrix. In the absence of an interphase region, one can identify two characteristic volume fractions; the CNT volume fraction within the matrix, $c_1 = r_1^2/r_2^2$, and the volume fraction of the hollow space within in the CNT, c_h, as given by $c_h = r_0^2/r_1^2$

It should also be noted that while the CC method has been used to predict effective composite properties out to very large volume fractions, again there is a limit on the highest attainable volume fraction as all of the nanotubes in the composite are assumed to be of the same size (the maximum packing volume fraction for identically sized aligned fibers is 90%). Results for volume fractions greater than 90% are shown to demonstrate that as the volume fraction approaches unity, i.e. the composite consists of carbon nanotubes only, that the properties returned are indeed those input for the effective CNT. Also of note, one could directly calculate concentration factors from the CC elasticity solutions and use either the Mori-Tanaka or self-consistent techniques with the advantage of more accurately accounting for the influence of multiple layers as opposed to using the effective CNT properties as is done herein for the CC/MT and CC/SC approaches. However, subsequent results will indicate that the CC/MT and CC/SC methods as applied herein are sufficiently accurate for the CNT reinforced composites studied.

Composite Cylinders Model for CNTs in the Presence of Interphase Regions

The effects of interphase regions on the effective properties of composites have been approached using a variety of techniques, mostly in the context of coated fiber inclusions(Benveniste et al., 1989, 1991; Dasgupta and Bhandarkar, 1992; Wagner, 1996; Anifantis et al., 1997; Wagner and Nairn, 1997; Benveniste and Miloh, 2001; Fisher and Brinson, 2001; Hashin, 2002). Herein the effects of interphase regions are modeled by taking advantage of the CC method. For cases with multiple types, sizes, and number of interphases as shown in Figure A.1 the CC/MT or CC/SC method can be used with P in Eqns. 2.1 and 2.3 equal to the number of different types of interphase arrangements with N_P indicating the last interphase

prior to the matrix and replacing N in the equations in Appendix A. For cases where all nanotubes are assumed to have the same interphase, the CC method can be used directly with N indicating the matrix so that N is equal to three or more in the equations in Appendix A. Though the size and material properties of interphase layers in CNT composites remain unknown, an effort to explore the effects of such an interphase layer using the CC method is accomplished herein.

Results of Modeling the Effective Elastic Properties of CNT Composites

The matrix material considered was EPON 862 and as previously stated, the CNTs were considered to be isotropic having the in-plane properties of graphene. The effective CNT properties as determined by the CC method for use in the CC/SC and CC/MT methods are given in Table 2.1 along the with isotropic properties of EPON 862. MWCNT values are also provided up to 10-wall CNTs demonstrating the more than two orders of magnitude difference between reinforcement and matrix properties.

Table 2.1. Elastic properties of EPON 862 and comparison of effective CNT axial and transverse Young's moduli for increasing number of perfectly bonded graphite layers. (Other effective CNT properties not shown)

Matrix: EPON 862		
$E = 3.07$ GPa	$\nu = 0.3$	
No. of Layers in Effective CNT	$\mathbf{E_{11}}$ **(GPa)**	$\mathbf{E_{22}}$ **(GPa)**
1	704	346
2	898	644
4	1018	887
6	1056	979
8	1073	1023
10	1081	1046

CC/SC results for bundles containing identical CNTs in the absence of any interphase region, i.e. P and N equal to one, are provided in Figure 2.3. The results shown are for the effective axial modulus, E_{11}, and the transverse modulus, E_{22}, for the complete range of volume fractions, c_1, of effective CNTs. One should note that for identical CNTs there are

geometric constraints restricting the maximum volume fraction to a value less than one, specifically, to a maximum value of approximately 90%. However, a range of CNT volume fractions up to one is used in the calculation for numerical completeness. It is worth mentioning that, even though E_{11} is greatly influenced by the presence of CNTs, the presence of the aligned CNTs is not evident in E_{22} until a very high volume fraction of about 60%. This is due to the nearly *two orders* of magnitude difference between the matrix Young's modulus and the effective nanotubes transverse modulus. The effective μ_{12}, μ_{23}, and κ_{23} elastic moduli display similar matrix dominated behavior as observed for E_{22}.

Figure 2.4 provides a comparison of the results obtained using the CC approach with both the CC/SC and CC/MT results also for bundles with identical CNTs and no interphase regions. Figure 2.4(a) demonstrates, as expected, that all three methods return the rule of mixtures for the effective axial modulus, E_{11}. However, for the remaining effective composite properties, the CC and CC/MT provide similar results whereas the CC/SC shows large differences at volume fractions greater then 60% relative to the other two methods as shown in Figure 2.4(b) for E_{22}. Moreover, this difference becomes more pronounced with increasing CNT volume fraction as the CC and CC/MT approaches demonstrates a higher degree of matrix dominance than does the CC/SC.

Figure 2.5 demonstrates the effects of changing the CNT to matrix stiffness ratio on the composite's effective E_{22} when normalized by the CNT's E_{22}. The original ratio, 1100:3, plus two other ratios obtained by holding the matrix value constant and spanning the range of published CNTs stiffness values are provided. As pointed out in Figure 2.5(b), the difference in the dominance of the matrix properties on the effective composite properties between the CC/SC and CC results shifts noticeably for the lower stiffness ratio cases. Specifically, the influence of CNTs at low volume fractions is more apparent as indicated by the increase in slope for the lower stiffness ratio results. In addition, the point at which a strong influence of CNTs is observed, i.e. where there is a large change in the slope of the curves shown in Figure 2.5, shifts to lower volume fractions for the lower stiffness ratio cases.

Comparison of finite element analysis (FEA) results with CC/SC, CC/MT, and CC results for identical CNTs in the absence of interphase regions are provided in Figure 2.6. The axial modulus, E_{11}, is not shown in Figure 2.6 as all methods (FEA, CC/SC, CC/MT, and CC) demonstrate the same linear response observed in Figure 2.4(a). Also not shown are the in-plane bulk modulus, κ_{23}, results as for the FEA results it is not an independent property (i.e. FEA obtains E_{11}, E_{22}, ν_{12}, μ_{12}, and μ_{23} independently and uses those to calculate κ_{23}). It should also be noted that FEA results were obtained using the actual hollow CNT geometry with the isotropic properties of graphene, as previously discussed, and arranged in a regular hexagonal array, shown in Figure 2.7, and subject to periodic boundary conditions on all six sides. The regular hexagonal array is known to produce effective properties which are transversely isotropic, as expected to be the case for random distributions of fibers in the transverse plane (Dvorak and Teply, 1985; Achenbach and Zhu, 1990). The large RVE chosen for the numerical examples is not the smallest for a perfect hexagonal array, but was chosen so as to be consistent with the clustering studies presented herein. In addition,

the same arrangement but with using solid transversely isotropic cylinders with effective CNT properties as obtained by the CC method in what could be termed a CC/FEA method was studied. FEA results for both cases were found to be in good agreement and as such, only the former are provided in Figure 2.6.

It is observed in Figure 2.6 that all methods compare favorably at low volume fractions. However, at volume fractions higher than 40%, where the CC/SC diverges from the other two analytic solutions, it is observed that the FEA results continue to compare well with the CC/MT and CC approaches. The CC/MT result is consistent with the general observation that the Mori-Tanaka method is more accurate for stiff fibers, and lends credence to the use of effective CNT properties in Mori-Tanaka methods for CNT composites and to the CC approach for aligned CNT composites.

The effects of interphase regions on the effective properties were studied using the CC approach. In each case, identical CNTs surrounded by a single interphase of a given thickness were considered so that N was equal to three with the first phase being the CNT and the N^{th} being the matrix. Parametric studies on the effects of having interphases with elastic modulus ranging from one tenth that of the matrix to ten times the matrix modulus and with thicknesses from half of a CNT radius to four times a CNT radius were studied and found to be negligible on E_{11} and ν_{12}. For E_{22}, μ_{12}, μ_{23}, and κ_{23} identical trends as shown for E_{22} in Figure 2.8 were observed. Figure 2.8 indicates that interphases with moduli less than that of the matrix are interphase dominated in the transverse direction so that there is virtually no noticeable presence of the CNTs in the effective properties until volume fractions very near unity. In contrast, interphases with moduli greater than that of the matrix greatly increase the effects of the presence of CNTs on the transverse properties even at very low volume fractions. Noticeable in Figures 2.8(a), 2.8(b), and 2.8(c) is a sharp change in the effective properties at specific volume fractions. The sharp transition in effective properties is directly attributed to the transition between having each CNT in the matrix surrounded by a distinct interphase to the volume fraction being sufficiently high such that the matrix volume fraction is zero, i.e. there is only CNT and interphase. Also observed, while a nearly three orders of magnitude difference between the matrix and CNTs exists, an interphase stiffness of only five times that of the matrix is enough to significantly improve the composite's effective properties. Similarly, an interphase whose stiffness is only half that of the matrix can significantly degrade the composite's effective properties.

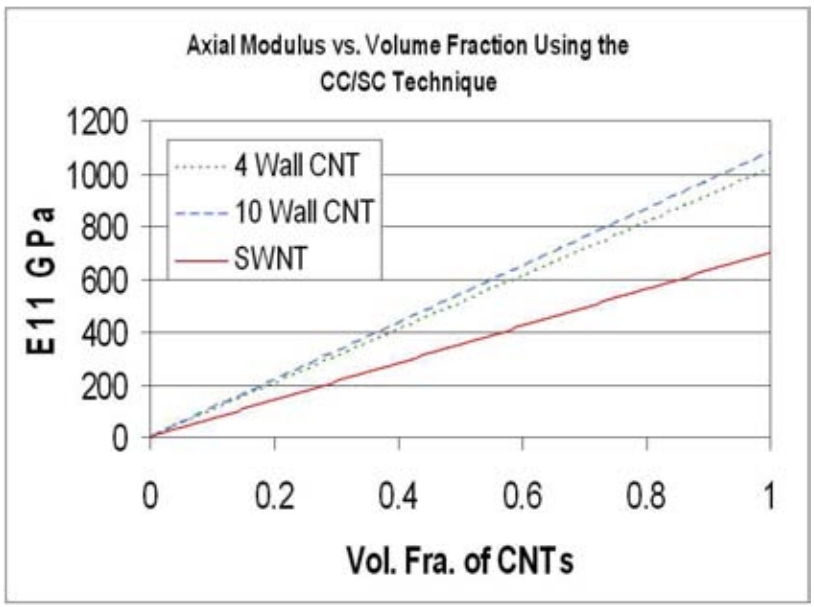

(a) Composite effective axial modulus, E_{11}, using CC/SC in the absence of interphase regions demonstrating CNT dominated behavior in the axial direction. Approach.

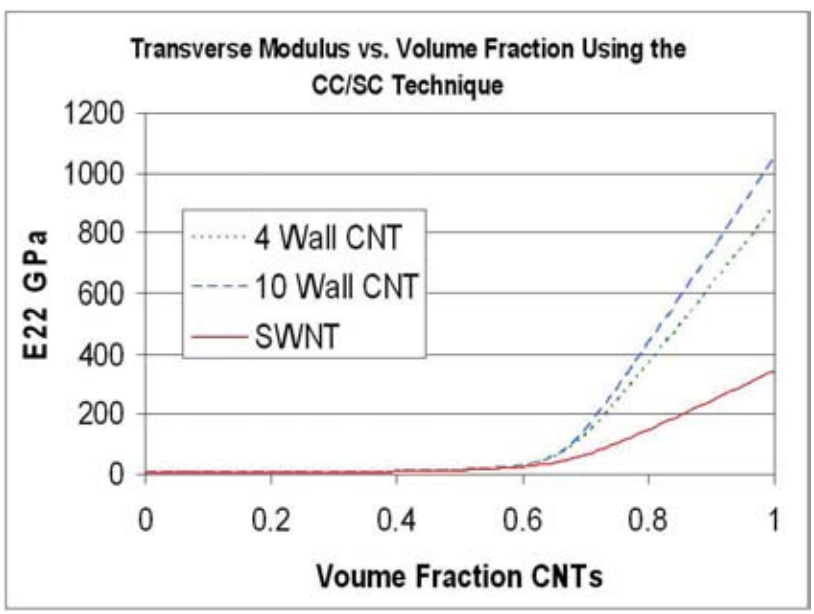

(b) Composite effective transverse modulus, E_{22}, using CC/SC in the absence of interphase regions demonstrating matrix dominated behavior in the transverse direction.

Figure 2.3. Effective axial and transverse moduli obtained via the CC/SC method.

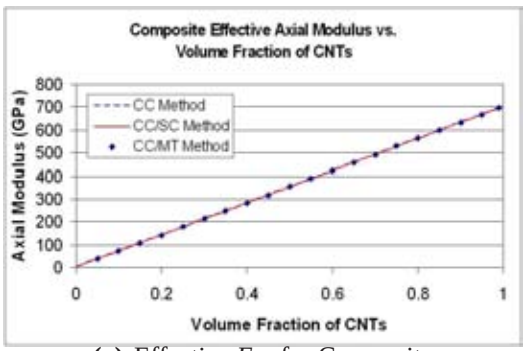

(a) Effective E_{11} for Composite

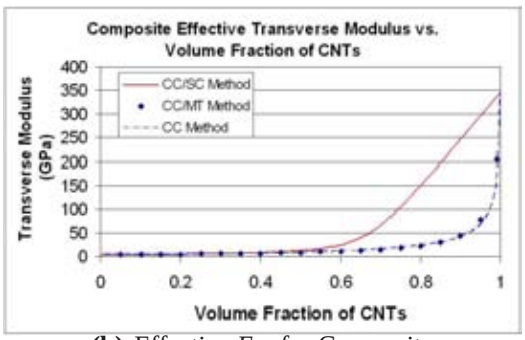

(b) Effective E_{22} for Composite

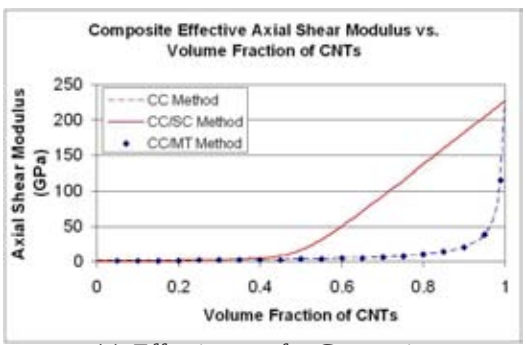

(c) Effective μ_{12} for Composite

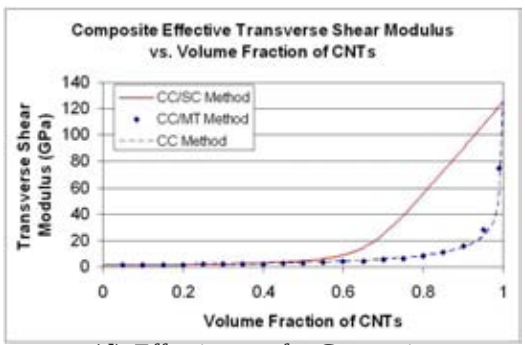

(d) Effective μ_{23} for Composite

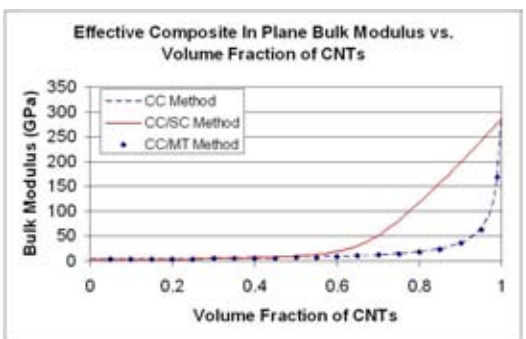

(e) Effective κ_{23} for Composite

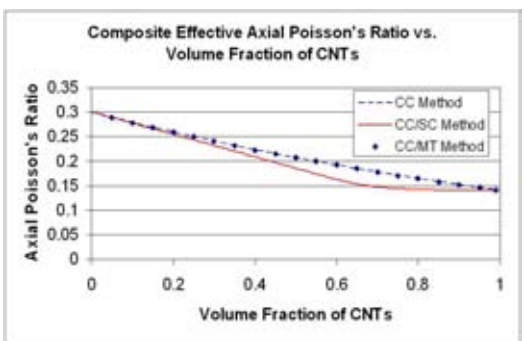

(f) Effective ν_{12} for Composite

Figure 2.4. Comparison of the CC/SC, CC/MT, and CC techniques for aligned CNT composites.

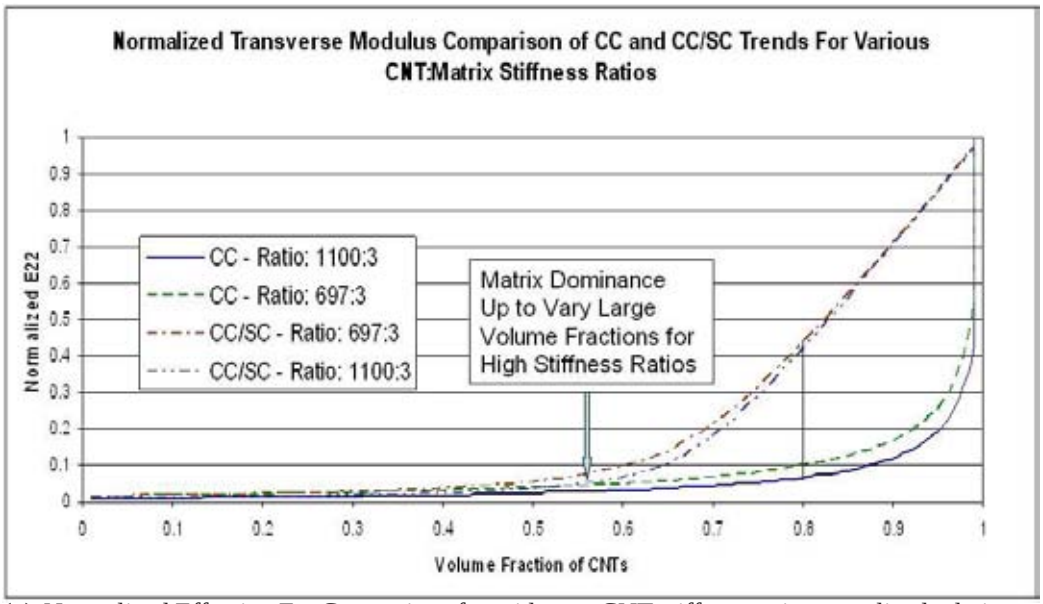

(a) Normalized Effective E_{22} Comparison for midrange CNT stiffness ratio normalized relative to the CNT effective transverse modulus.

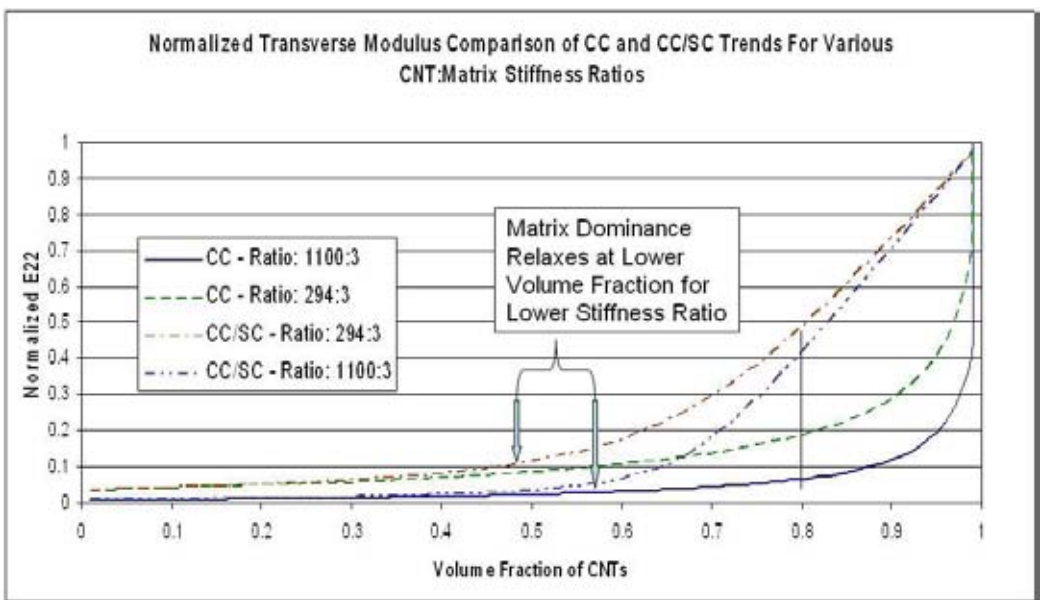

(b) Normalized Effective E_{22} Comparison for low end CNT stiffness ratio normalized relative to the CNT effective transverse modulus

Figure 2.5. Parametric study on CNT to Matrix Stiffness Ratio: Comparison of the CC/SC and CC Techniques for Aligned Composites.

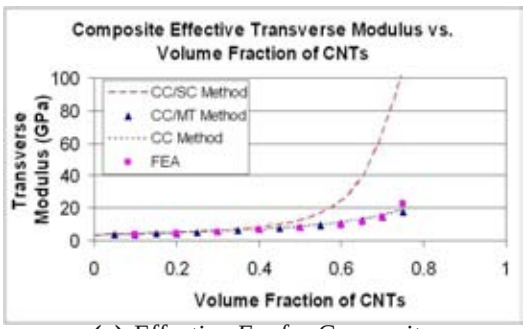

(a) Effective E_{22} for Composite

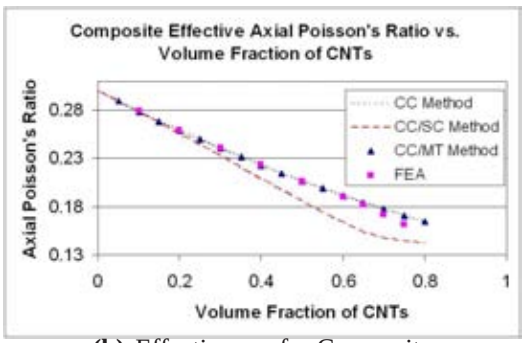

(b) Effective ν_{12} for Composite

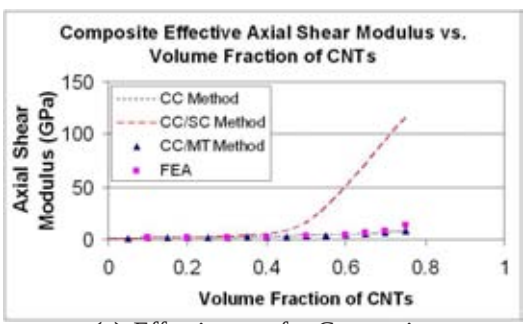

(c) Effective μ_{12} for Composite

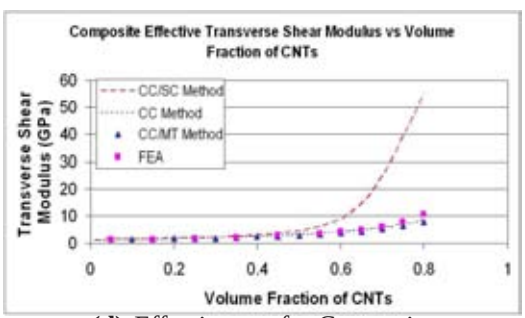

(d) Effective μ_{23} for Composite

Figure 2.6. Comparison of the CC/SC, CC/MT, and CC techniques to FEA Solutions. CC/MT and CC show excellent agreement with FEA solutions. FEA solutions were obtained using CNTs and effective CNTs arranged in a regular hexagonal array and subject to periodic boundary conditions.

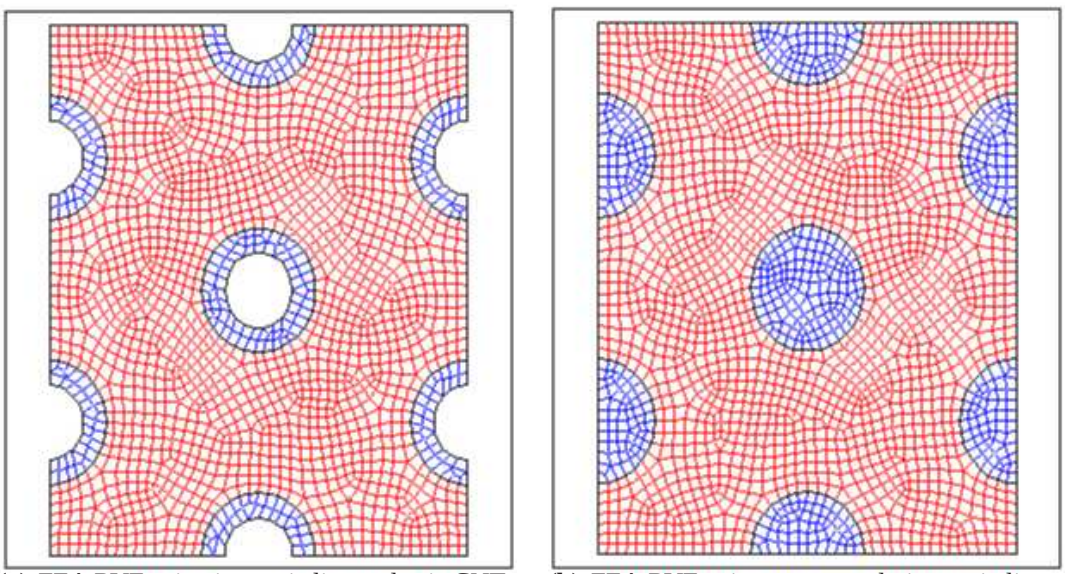

(a) FEA RVE using isotropic linear elastic CNTs

(b) FEA RVE using transversely isotropic linear elastic effective CNTs

Figure 2.7. FEA RVE's used to generate effective composite properties.

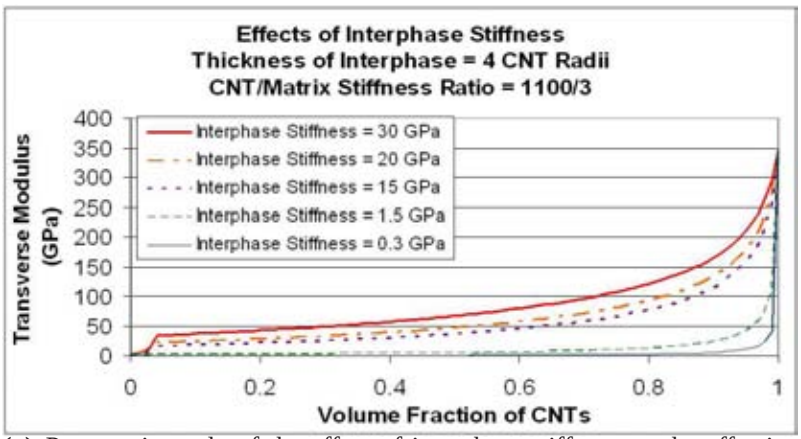

(a) Parametric study of the effect of interphase stiffness on the effective transverse modulus for an interphase thickness of 4 CNT radii

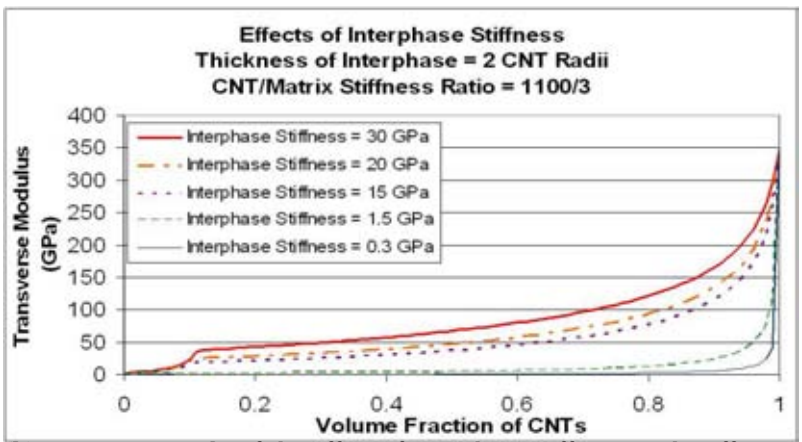

(b) Parametric study of the effect of interphase stiffness on the effective transverse modulus for an interphase thickness of 2 CNT radii

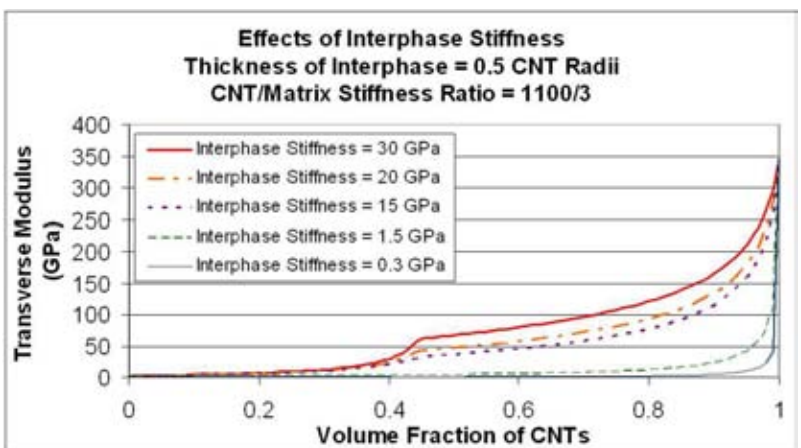

(c) Parametric study of the effect of interphase stiffness on the effective transverse modulus for an interphase thickness of half a CNT radius

Figure 2.8. Parametric Study on the effects of interphase thickness and stiffness on the effective properties of CNT reinforced composites using the CC technique with N=3 (i.e. CNT, interphase, and matrix).

Chapter 3

Computational Micromechanics Approach

Problem Statement and Computational Approach

In the present work, the finite element method will be used to determine effective elastic properties corresponding to aligned high-stiffness hollow fibers embedded in a compliant matrix in both well-dispersed and clustered arrangements. The configuration considered for the well-dispersed case is assumed to consist of a periodic hexagonal array of hollow fibers (Figure 3.1(a)), resulting in effective material behavior which is transversely isotropic (Dvorak and Teply, 1985; Achenbach and Zhu, 1990). Clustering is considered by allowing different degrees of deviation from the periodic hexagonal array, as shown in Figure 3.1(b). Also shown in Figure 3.1 are the interphase regions surrounding the fibers which are assumed to be of uniform size and stiffness. The interphase regions are also assumed to be perfectly bonded to both the fibers and the matrix. The material properties for both the hollow fibers and the matrix are taken to be linear elastic. In both the well-dispersed and clustered cases, the equilibrium equations are numerically solved using FEA, subject to periodic boundary conditions.

In order to capture both the well-dispersed and clustered cases, the elastic properties of the effective homogeneous material are assumed to be orthotropic linear elastic, which can be expressed in terms of the components of the stiffness tensor as

$$\begin{Bmatrix} \bar{\sigma}_{11} \\ \bar{\sigma}_{22} \\ \bar{\sigma}_{33} \\ \bar{\sigma}_{12} \\ \bar{\sigma}_{23} \\ \bar{\sigma}_{31} \end{Bmatrix} = \begin{bmatrix} C_{11} & C_{12} & C_{13} & 0 & 0 & 0 \\ C_{12} & C_{22} & C_{23} & 0 & 0 & 0 \\ C_{13} & C_{23} & C_{33} & 0 & 0 & 0 \\ 0 & 0 & 0 & C_{44} & 0 & 0 \\ 0 & 0 & 0 & 0 & C_{55} & 0 \\ 0 & 0 & 0 & 0 & 0 & C_{66} \end{bmatrix} \begin{Bmatrix} \bar{\varepsilon}_{11} \\ \bar{\varepsilon}_{22} \\ \bar{\varepsilon}_{33} \\ 2\bar{\varepsilon}_{12} \\ 2\bar{\varepsilon}_{23} \\ 2\bar{\varepsilon}_{31} \end{Bmatrix} \tag{3.1}$$

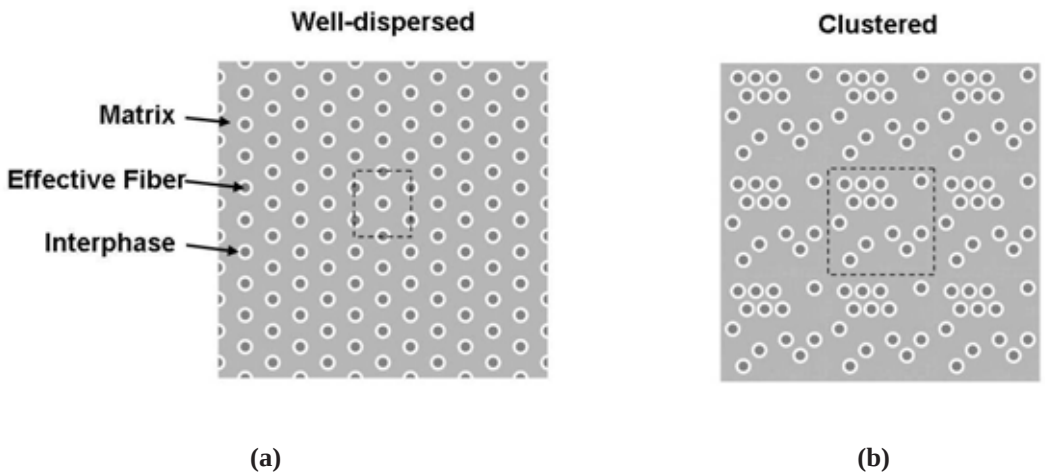

Figure 3.1. Schematic of effective fiber FEA representations of aligned high-stiffness hollow fibers embedded in a matrix with fiber-matrix interphase regions: (a) well-dispersed case (perfect hexagonal array); (b) a clustered case. Both schematics are plotted using the same geometrical scale and both correspond to 10% volume fraction of fibers and 10% volume fraction of interphase regions. Dashed lines denote the computational representative volume elements for each case.

or inverted and expressed in terms of the components of the compliance tensor as

$$\begin{Bmatrix} \bar{\varepsilon}_{11} \\ \bar{\varepsilon}_{22} \\ \bar{\varepsilon}_{33} \\ 2\bar{\varepsilon}_{12} \\ 2\bar{\varepsilon}_{23} \\ 2\bar{\varepsilon}_{31} \end{Bmatrix} = \begin{bmatrix} \frac{1}{E_{11}} & -\frac{\nu_{21}}{E_{22}} & -\frac{\nu_{31}}{E_{33}} & 0 & 0 & 0 \\ -\frac{\nu_{12}}{E_{11}} & \frac{1}{E_{22}} & -\frac{\nu_{32}}{E_{33}} & 0 & 0 & 0 \\ -\frac{\nu_{13}}{E_{11}} & -\frac{\nu_{23}}{E_{22}} & \frac{1}{E_{33}} & 0 & 0 & 0 \\ 0 & 0 & 0 & \frac{1}{G_{12}} & 0 & 0 \\ 0 & 0 & 0 & 0 & \frac{1}{G_{23}} & 0 \\ 0 & 0 & 0 & 0 & 0 & \frac{1}{G_{31}} \end{bmatrix} \begin{Bmatrix} \bar{\sigma}_{11} \\ \bar{\sigma}_{22} \\ \bar{\sigma}_{33} \\ \bar{\sigma}_{12} \\ \bar{\sigma}_{23} \\ \bar{\sigma}_{31} \end{Bmatrix} \tag{3.2}$$

where $\bar{\sigma}_{ij}$ are the components of the volume averaged stress, $\bar{\varepsilon}_{ij}$ are the average components of strain applied to the RVE, and where the E's, ν's, and G's denote effective Young's moduli, Poisson's ratios, and shear moduli, respectively. Of course, the usual material parameter symmetries hold (i.e., $\frac{\nu_{21}}{E_{22}} = \frac{\nu_{12}}{E_{11}}$, $\frac{\nu_{31}}{E_{33}} = \frac{\nu_{13}}{E_{11}}$, and $\frac{\nu_{32}}{E_{33}} = \frac{\nu_{23}}{E_{22}}$). For the well-dispersed case only five of the effective elastic constants are independent as the effective material response is transversely isotropic. The effective elastic properties are obtained through the application of a series of average strain states, each having a single non-zero component. The resulting sets of volume averaged stress components for a an applied average strain are then determined from the FEA solution, allowing the components of the corresponding column of the effective stiffness matrix in Eqn. 3.1 to be obtained by dividing the average stress components by the applied average strain. Once the effective stiffness is computed, it is inverted to obtain the effective compliance from which the corresponding engineering effective elastic constants are determined according to Eqn. 3.2.

In the finite element simulations which follow, it is assumed that the fibers are infinitely long circular cylinders, consistent with the large aspect ratio of CNTs (Saito et al., 1998). Earlier work of Fisher et al. (2002) has accounted for the effect of curvature of CNTs on the effective elastic properties, where it was shown to cause a reduction in modulus on the order 5% relative to straight fibers. In the present work, emphasis is placed on the effects of clustering and interphase regions and, for the simplicity of computations, straight fibers will be considered. Two continuum representations of CNTs are employed in the present work. In the first representation, CNTs are treated as isotropic linear elastic hollow fibers, consistent with the identification of CNTs as rolled sheets of graphite (Saito et al., 1998). In the second, CNTs are represented as transeversely isotropic linear elastic solid fibers with the effective elastic constants for the fibers determined using a composites cylinders method (Seidel and Lagoudas, 2006a). In all cases, the matrix and interphase regions are taken to be linear elastic isotropic. Relevant geometric data and material properties for the CNT representations and for the epoxy matrix are provided in Table 3.1. Interphase properties are taken as a variable in the present work and are provided on a case-by-case basis. Also note that in both hollow and effective fiber FEA representations, volume fraction is measured using a fiber radius equal to the outer radius identified in Table 3.1 (i.e., the hollow portion is considered part of the fiber volume in the hollow fiber FEA representation).

Table 3.1. Linear elastic material parameters for continuum representations of CNTs using isotropic hollow fibers or transversely isotropic effective fibers. Elastic properties for the epoxy matrix along with geometrical dimensions of the CNT representations are also provided.

Matrix: EPON 828 (Schadler et al., 1998)	
$E = 3.07$ GPa	$\nu = 0.3$

Isotropic Hollow Fiber FEA Representation of CNT (Saito et al., 1998)	
$E = 1100$ GPa	$\nu = 0.14$
Inner Radius $= 0.51$ nm	Outer Radius $= 0.85$ nm

Transversely Isotropic Effective Fiber FEA Representation of CNT (Seidel and Lagoudas, 2006a)	
$E_{11} = 704$ GPa	$E_{22} = 345.54$ GPa
$G_{12} = 227.04$ GPa	$G_{23} = 125.52$ GPa
$\nu_{12} = 0.14$ GPa	Outer Radius $= 0.85$ nm

Examples of the RVEs used for the well-dispersed and clustered fiber arrangements in the finite element computations which follow are denoted by the dashed lines in Figure 3.1. Although it is possible to use a much smaller RVE for the well-dispersed case (e.g., one-sixth of a hexagonal prism centered about a fiber), the chosen RVE results in straightforward specification of the necessary periodic boundary conditions. The computational cost associated with using these rectangular RVEs is not burdensome and allows similar boundary conditions to be used for both the well-dispersed and clustered fiber arrangements. Both the well-dispersed and clustered computational RVEs are assumed to possess a translational periodicity in the X- and Y-directions, with vectors of periodicity being defined by the size of the RVE.

Sample meshes of the well-dispersed RVE for both the hollow and effective fiber CNT representations are shown in Figure 3.2. These meshes are three-dimensional with a single element used in the Z-direction, which is sufficient as no gradients in the Z-direction result when the periodic boundary conditions are applied. New meshes are generated for each fiber volume fraction for which the effective elastic properties are determined. As the fiber dimensions are considered to be fixed, changes in fiber volume fraction result in changes in the size of the RVE.

In order to facilitate the discussion of the applied periodic boundary conditions, the six faces will be referred to as $+X/-X$, $+Y/-Y$, and $+Z/-Z$ which are perpendicular to the X-, Y-, and Z-axes, respectively. Also, a numbering scheme will be used for the principal material directions such that 1 refers to the fiber axis direction (Z-axis) and 2 and 3 correspond to the X- and Y-axes, respectively, or the transverse axes. A total of six numerical simulations are used to determine the effective composite properties at a given fiber volume fraction for both the well-dispersed and clustered fiber arrangements. Each simulation corresponds to the application of an average strain state with a single non-zero component. These six simulations are necessary to determine the complete set of engineering elastic constants of an orthotropic material, i.e., the three Young's moduli (E_{11}, E_{22}, and E_{33}), the three Poisson's ratios (ν_{12}, ν_{23}, and ν_{31}) and the three shear moduli (G_{12}, G_{23}, and G_{31}), from which all other effective moduli can be calculated. It should be noted that in the well-dispersed case, where the effective elastic properties are transversely isotropic, only three simulations are needed to obtain the five independent engineering properties. The additional three tests become consistency checks for the well-dispersed cases.

The periodic boundary conditions can be expressed in terms of the displacement components on face pairs. For example, taking the origin of the mesh coordinate system to be at the RVE centroid, the periodic conditions for the $+X/-X$ face pair can be expressed as:

$$\begin{aligned} u(L_X^o/2,Y,Z) &= u(-L_X^o/2,Y,Z) \\ v(L_X^o/2,Y,Z) &= v(-L_X^o/2,Y,Z) \\ w(L_X^o/2,Y,Z) &= w(-L_X^o/2,Y,Z) \end{aligned} \tag{3.3}$$

where u, v, and w are the components of the displacement in the X, Y, and Z directions, respectively, and where the undeformed mesh has an original length along the X-axis of

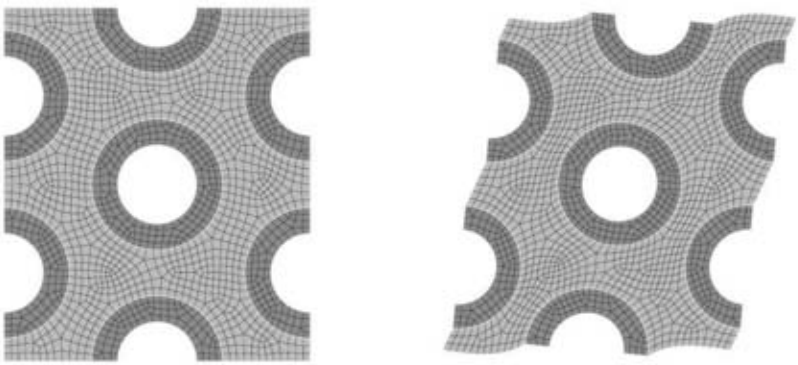

(a)

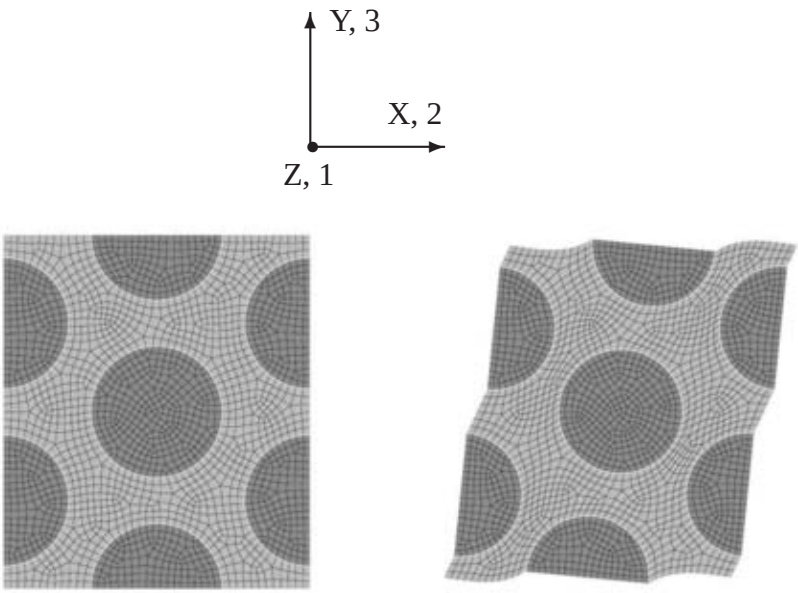

(b)

Figure 3.2. Original and deformed finite element meshes for aligned, well-dispersed hollow fiber (3554 nodes/1648 elements) and effective fiber (4496 nodes/2154 elements) representations at 50% volume fraction. Here the interphase region has been assigned the same properties as the matrix indicative of direct fiber-matrix bonding; (a) isotropic hollow fiber FEA representation; (b) transversely isotropic effective fiber FEA representation. The deformed meshes are for the case of applied shear, $\overline{\gamma}_{23}$, of 1%, with 20X displacement magnification demonstrating that straight edges are not required to remain straight for the applied periodic boundary conditions.

L_X^o. Similarly, on the $+Y/-Y$ and $+Z/-Z$ face pairs, the periodic conditions are expressed as:

$$\begin{aligned} u(X, L_Y^o/2, Z) &= u(X, -L_Y^o/2, Z) \\ v(X, L_Y^o/2, Z) &= v(X, -L_Y^o/2, Z) \\ w(X, L_Y^o/2, Z) &= w(X, -L_Y^o/2, Z) \end{aligned} \tag{3.4}$$

and

$$\begin{aligned} u(X, Y, L_Z^o/2) &= u(X, Y, -L_Z^o/2) \\ v(X, Y, L_Z^o/2) &= v(X, Y, -L_Z^o/2) \\ w(X, Y, L_Z^o/2) &= w(X, Y, -L_Z^o/2) \end{aligned} \tag{3.5}$$

respectively, and where the undeformed mesh has original lengths of L_Y^o, and L_Z^o along the Y and Z coordinate axes. In order to perform one of the required six numerical simulations, the desired non-zero average strain component is introduced into the periodic conditions in the form of a relative displacement. For example, in order to determine the first column of the stiffness tensor in Eqn. 3.1, the only non-zero average strain, $\bar{\varepsilon}_{11}$, is applied by the addition of a relative displacement between $+Z$ and $-Z$ in the w component of Eqn. 3.5, i.e.,

$$w(X, Y, L_Z^o/2) = w(X, Y, -L_Z^o/2) + \varepsilon^o L_Z^o \tag{3.6}$$

where the relative displacement is given by $w_{rel} = \varepsilon^o L_Z^o$, where ε^o is the applied strain. For this case, the remaining displacement components in Eqn. 3.5 are unaltered, and the same is true of all of the displacement components in Eqns. 3.3 and 3.4. The other columns of the stiffness tensor are determined in much the same way, with the only difference being to which face and to which displacement component a relative displacement is applied. The specifics of the periodic boundary conditions (PBCs) used in each simulation to apply the desired component of average strain ($\bar{\varepsilon}_{ij}$) are listed in Table 3.2, where the corresponding relative displacements are denoted by u_{rel}, v_{rel}, and w_{rel}. Note that most nodes belong to a single PBC pair ($+Z/-Z$), while some belong to two PBC pairs ($+Z/-Z$ with either $+X/-X$ or $+Y/-Y$) and the eight corner nodes belong to all three PBC pairs. Also note that the inner surface of the fiber in the hollow fiber FEA representation of the CNTs is taken to be stress free. Finally, note that initially straight edges need not remain straight under the applied periodic boundary conditions as is also shown in Figure 3.2.

The finite element cases are run with ADAGIO (Pierson et al., 2005), Sandia National Laboratories' finite element software for linear and nonlinear quasi-static analysis of structures. ADAGIO solves the following weak form in the current configuration

$$\int_V \boldsymbol{\sigma} : \delta\mathbf{D}\, dV = \int_V \rho\mathbf{b} \cdot \delta\mathbf{v}\, dV + \int_S \mathbf{t} \cdot \delta\mathbf{v}\, dS \tag{3.7}$$

where $\boldsymbol{\sigma}$ is the Cauchy stress tensor in the current configuration, $\mathbf{D}$ is the rate-of-deformation tensor, $\mathbf{b}$ is the body force vector, $\mathbf{v}$ is the velocity vector, and $\mathbf{t}$ is the traction vector. Many

Table 3.2. Details of applied periodic boundary conditions. The non-zero relative displacements necessary to achieve the desired average strain over the RVE are given. All unlisted relative displacements are specified to be zero. In all numerical simulations for a given RVE, a single applied strain level of ε^o is used and L_X^o, L_Y^o, and L_Z^o refer to undeformed RVE lengths in the X-, Y-, and Z-directions, respectively, and u_{rel}, v_{rel}, and w_{rel} are the corresponding relative displacements.

Simulation	Average Applied Strain	$+X/-X$ PBC	$+Y/-Y$ PBC	$+Z/-Z$ PBC
1. Z-Direction Extension	$\bar{\varepsilon}_{11} = \bar{\varepsilon}_{zz} = \varepsilon^o$	–	–	$w_{rel} = \varepsilon^o L_Z^o$
2. X-Direction Extension	$\bar{\varepsilon}_{22} = \bar{\varepsilon}_{xx} = \varepsilon^o$	$u_{rel} = \varepsilon^o L_X^o$	–	–
3. Y-Direction Extension	$\bar{\varepsilon}_{33} = \bar{\varepsilon}_{yy} = \varepsilon^o$	–	$v_{rel} = \varepsilon^o L_Y^o$	–
4. ZX Shear	$2\bar{\varepsilon}_{12} = 2\bar{\varepsilon}_{zx} = \varepsilon^o$	$w_{rel} = \varepsilon^o L_X^o$	–	–
5. XY Shear	$2\bar{\varepsilon}_{23} = 2\bar{\varepsilon}_{xy} = \varepsilon^o$	–	$u_{rel} = \varepsilon^o L_Y^o$	–
6. YZ Shear	$2\bar{\varepsilon}_{31} = 2\bar{\varepsilon}_{yz} = \varepsilon^o$	–	$w_{rel} = \varepsilon^o L_Y^o$	–

different types of constitutive equations are available in ADAGIO. For the present application, the Green-Naghdi objective stress rate is used and is given by

$$\overset{\circ}{\sigma} = \dot{\sigma} - \Omega\sigma + \sigma\Omega \tag{3.8a}$$

or

$$\overset{\circ}{\sigma} = \mathbf{R}\,\dot{\sigma}^u\,\mathbf{R}^T \tag{3.8b}$$

where $\mathbf{R}$ is the rotation matrix from the polar decomposition of the total deformation gradient $\mathbf{F}$, i.e., $\mathbf{F} = \mathbf{RU} = \mathbf{VR}$ with $\mathbf{U}$ and $\mathbf{V}$ denoting the total right and left stretch tensors, respectively, Ω is determined from the time rate of change of $\mathbf{R}$ as

$$\Omega = \dot{\mathbf{R}}\mathbf{R}^T \tag{3.9}$$

and σ^u is the unrotated Cauchy stress given by

$$\sigma^u = \mathbf{R}^T\sigma\mathbf{R} \tag{3.10}$$

Using Eqn. 3.8b, the constitutive equation is more easily applied directly in the unrotated configuration as follows:

$$\dot{\sigma}^u = \mathbf{C}^u\,\mathbf{D}^u \tag{3.11}$$

where $\mathbf{D}^u$ is the unrotated rate-of-deformation tensor given by

$$\mathbf{D}^u = \mathbf{R}^T\,\mathbf{D}\,\mathbf{R} \tag{3.12}$$

and $\mathbf{C}^u$ is the corresponding stiffness tensor.

ADAGIO solves for the nodal velocities satisfying the weak form given in Eqn. 3.7 using a nonlinear preconditioned conjugate gradient technique. That is, for each time step, ADAGIO begins with an initial guess for the nodal velocities and then iteratively finds the set of nodal velocities that satisfy the quasi-static equilibrium equations. The nodal velocities themselves are used to update the nodal displacements such that all quantities of interest can be computed in the displacement based finite element approach that is applied. The rate-of-deformation tensor is determined as follows:

$$\mathbf{D} = -\frac{1}{\Delta t} \ln \hat{\mathbf{V}}^{-1} \tag{3.13}$$

where $\hat{\mathbf{V}}$ is the incremental left stretch tensor computed from the polar decomposition of the incremental deformation gradient tensor over the current time step (i.e., $\hat{\mathbf{F}} = \hat{\mathbf{V}}\hat{\mathbf{R}}$). The unrotated rate-of-deformation tensor is then determined from Eqn. 3.12, where it should be noted that $\mathbf{R}$ is the total rotation from the initial undeformed configuration to the current configuration, and not the rotation from the previous configuration to the current one, i.e., not $\hat{\mathbf{R}}$. Once Eqn. 3.11 is used to update the unrotated Cauchy stress, the inverse of Eqn. 3.10 is used to obtain the Cauchy stress in the current configuration. The resulting internal force is compared to the external force to calculate a residual which is driven to zero. That is, if the residual is too large, a new nodal velocity vector is determined using a nonlinear preconditioned conjugate gradient method and the process is repeated until the residual is less than a user specified tolerance.

It should be noted that ADAGIO offers a range of elements, but here the computations are performed using the under-integrated, mean quadrature 8-node brick element. The hourglass modes are controlled via a fictitious hourglass force scheme similar to that described in Flanagan and Belytschko (1981) and Flanagan (1983).

It should also be noted that for the three extension tests listed in Table 3.2, the rotation tensor is equal to the identity tensor, i.e., $\mathbf{R} = \mathbf{I}$. For the three shear tests, the rotation is approximately equal to the identity tensor for the small strains applied in the PBCs. Hence, with the various rotated and unrotated tensors being nearly equal, it can be shown that the equations solved by ADAGIO reduce to the usual linearized elasticity equations. That is, for the small strain cases applied, the equations solved by ADAGIO are consistent with solving the quasi-static equilibrium equations given by

$$\nabla \cdot \sigma + \rho \mathbf{b} = \mathbf{0} \tag{3.14}$$

subject to the following linear elastic constitutive relationship:

$$\sigma = \mathbf{C}\, \varepsilon \tag{3.15}$$

where $\mathbf{C}$ is the usual engineering stiffness tensor (which is isotropic for the matrix and for the hollow fiber FEA representation and is transversely isotropic for the effective fiber FEA representation) and ε is the small strain tensor given by

$$\varepsilon = \frac{1}{2}\left(\nabla \mathbf{u} + (\nabla \mathbf{u})^T\right) \tag{3.16}$$

which is indicative of kinematic linearization.

The finite element results will be compared to solutions determined using analytic micromechanics techniques in the form of the multi-layered composite cylinders approach (Seidel and Lagoudas, 2006a) which is briefly summarized in Appendix A. In this approach, a single hollow fiber representation of the CNT, surrounded by concentric cylinders of interphase, matrix, and as yet to be determined effective material, constitutes the composite cylinder assemblage which is used to determine the effective composite properties. Different sets of boundary conditions are applied to the composite cylinder assemblage, and the five independent effective elastic constants are obtained by equating the strain energy of the composite cylinder assemblage with the strain energy of an equivalent effective solid. Details of the approach as applied to the composite system studied herein to investigate clustering and interphase effects can be found in previous work by Seidel and Lagoudas (2006a).

Effective Elastic Properties of Well-Dispersed Hollow Fiber Composites with Interphase Regions

Effective elastic properties for aligned, well-dispersed hollow fibers with interphase regions are obtained using both analytic and computational micromechanics approaches. In order to provide a reference for observing the effects of interphase regions, no-interphase cases are also performed. Finite element results for the effective elastic properties of hollow and effective fiber FEA representations for the well-dispersed case are provided in Figure 3.3. Also included in the plots are the effective properties obtained using the composite cylinders technique (Seidel and Lagoudas, 2006a). Even though, for completeness, results for fiber volume fractions up to 90% (the maximum packing fraction) are shown in Figure 3.3, it should be noted that current fabrication methods for CNT-epoxy composites typically have CNT volume fractions which are less than 10% Zhu et al. (2004).

As shown in Figure 3.3(a), the effective axial modulus, E_{11}, for both finite element representations and for the composite cylinders solution compare very favorably throughout the complete range of volume fractions. As is expected to be the case for fibrous composites, the effective elastic axial modulus is well approximated by a linear function of volume fraction between the fiber and matrix stiffnesses (i.e., rule of mixtures). Figure 3.3(b) provides the effective transverse modulus, E_{22}, where again good agreement between both of the finite element representations and the composite cylinders solution is observed for fiber volume fractions less than 60%. At fiber volume fractions greater than 60%, increasing differences in effective E_{22} are seen, with the effective fiber FEA representation demonstrating the largest effective stiffness followed by the hollow fiber FEA representation and then the composite cylinder solution. The difference in effective transverse modulus between the effective fiber FEA representation and the composite cylinder solution is noted to be of the order of 15% at a fiber volume fraction of 80%.

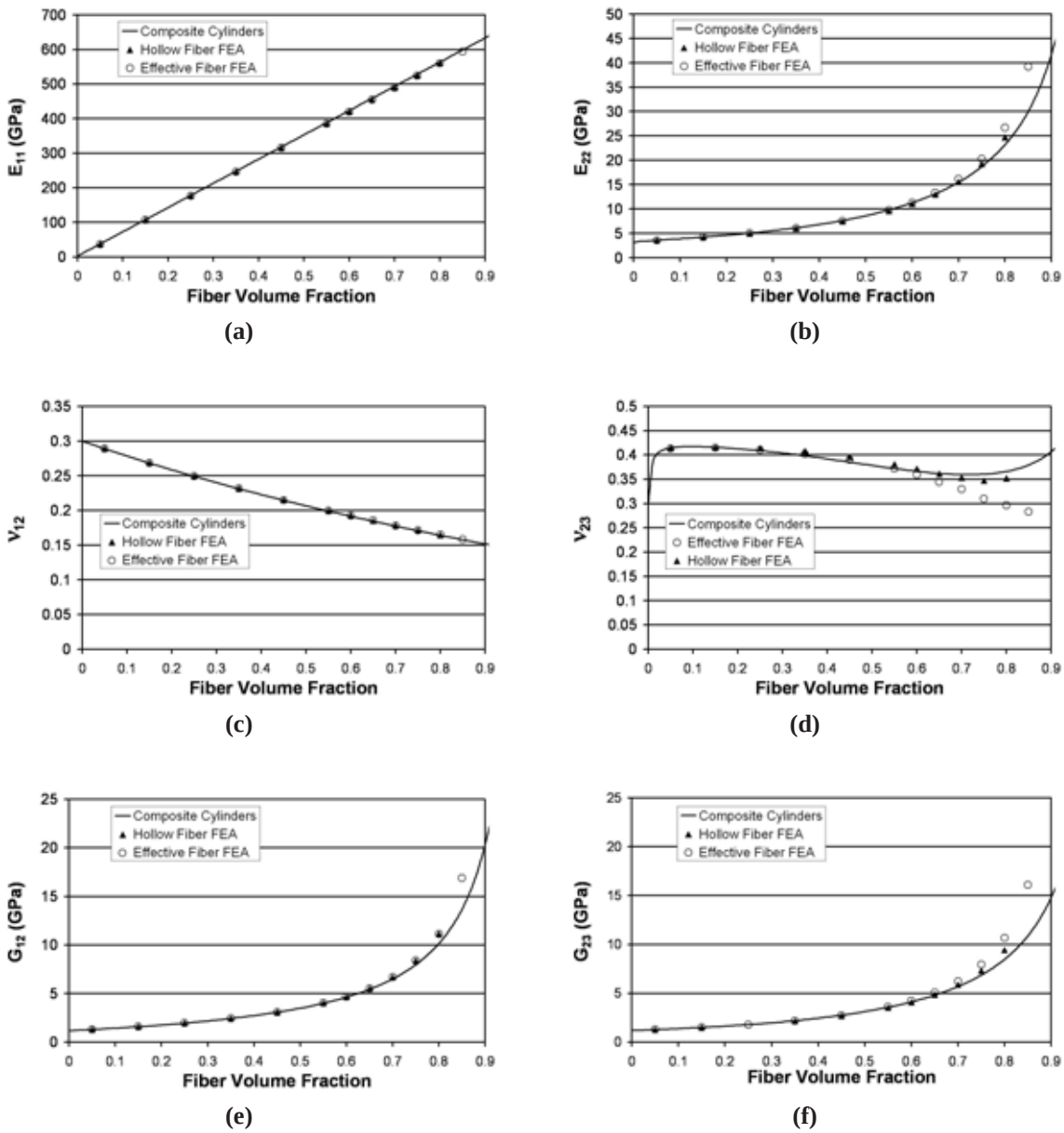

Figure 3.3. Comparison of finite element results with those obtained by the composite cylinders solutions for the well-dispersed case with the interphase having been replaced with matrix indicative of direct fiber-matrix bonding: (a) Axial Modulus, E_{11}; (b) Transverse Modulus, E_{22}; (c) ν_{12} Poisson's Ratio; (d) ν_{23} Poisson's Ratio; (e) G_{12} Shear Modulus; (f) G_{23} Shear Modulus.

Similar trends are observed in the Poisson's ratios. That is, for the effective ν_{12} Poisson's ratio, shown in Figure 3.3(c), all solutions compare favorably throughout the complete range of volume fractions. However, for the ν_{23} Poisson's ratio, large differences between the results from the two computational and the analytic solution methods again begin around 60% fiber volume fraction as shown Figure 3.3(d). Of particular note in Figure 3.3(d) is the more pronounced difference between the hollow and effective fiber FEA representations at high volume fractions. Here the effective fiber FEA representation does not adequately account for the zero-stiffness hollow region of the fiber which has increasing influence in the transverse properties at high fiber volume fractions.

Whereas the effective moduli and Poisson's ratios displayed dissimilar trends compared to one another (i.e., E_{11} vs. E_{22} and ν_{12} vs. ν_{23}), the effective shear moduli, G_{12} and G_{23}, results shown in Figures 3.3(e) and 3.3(f), respectively, are quite similar. Both shear moduli show initially good agreement between all three solution approaches up to 60% fiber volume fraction, and both show differences in effective shear moduli at larger fiber volume fractions. In fact, both effective shear moduli plots demonstrate a similar increase in effective property with increasing fiber volume fraction as that observed for the effective transverse modulus in Figure 3.3(b), where the increase in effective property is relatively small initially before increasing rapidly after 60% fiber volume fraction. As such, compared to the effective axial modulus and the ν_{12} Poisson's ratio, which show an almost rule of mixtures change in effective property with increasing fiber volume fraction, the G_{12} shear modulus is observed to be much more sensitive to the compliant nature of the matrix material. Though the shear moduli show similar trends, the effective G_{12} are results are larger in value and show less difference between solution methods at high fiber volume fractions than do the effective G_{23} results due to the reinforcing effect of the fibers being aligned in the 1-direction.

Reasons for the differences in the effective elastic properties observed in Figure 3.3 can best be understood by examining the associated stress distributions. Stress distribution contour plots for the well-dispersed, no interphase effective fiber finite element representation results are provided in Figure 3.4 for fiber volume fractions of 20% and 70% ($V_f = 0.2$ and 0.7). In both cases, the applied average strain, $\overline{\varepsilon}_{ij}$, is 1%, and the stress distributions have been plotted with a single contrast value used for each element, consistent with the under-integrated, mean quadrature 8-node brick element employed.

In Figure 3.4(a), stress contours of axial stress, σ_{11}, as a result of applied average axial strain, $\overline{\varepsilon}_{11}$, indicate that the effective fibers carry the majority of the load at all volume fractions. In fact, the stress level in the effective fibers and in the matrix remain constant at all volume fractions so that as the fiber volume fraction is increased, the average stress in the composite is proportionally increased resulting in the good agreement with the rule of mixtures response previously noted for the axial modulus, E_{11}. In contrast, Figures 3.4(b) and 3.4(c), which provide the stress contours associated with the determination of the transverse modulus, E_{22}, and the G_{23} shear, respectively, show an increasing amount of effective fiber interaction with increasing fiber volume fraction, as indicated by the increased stress state in both the fibers and the matrix at 70% volume fraction. It is this increase in the

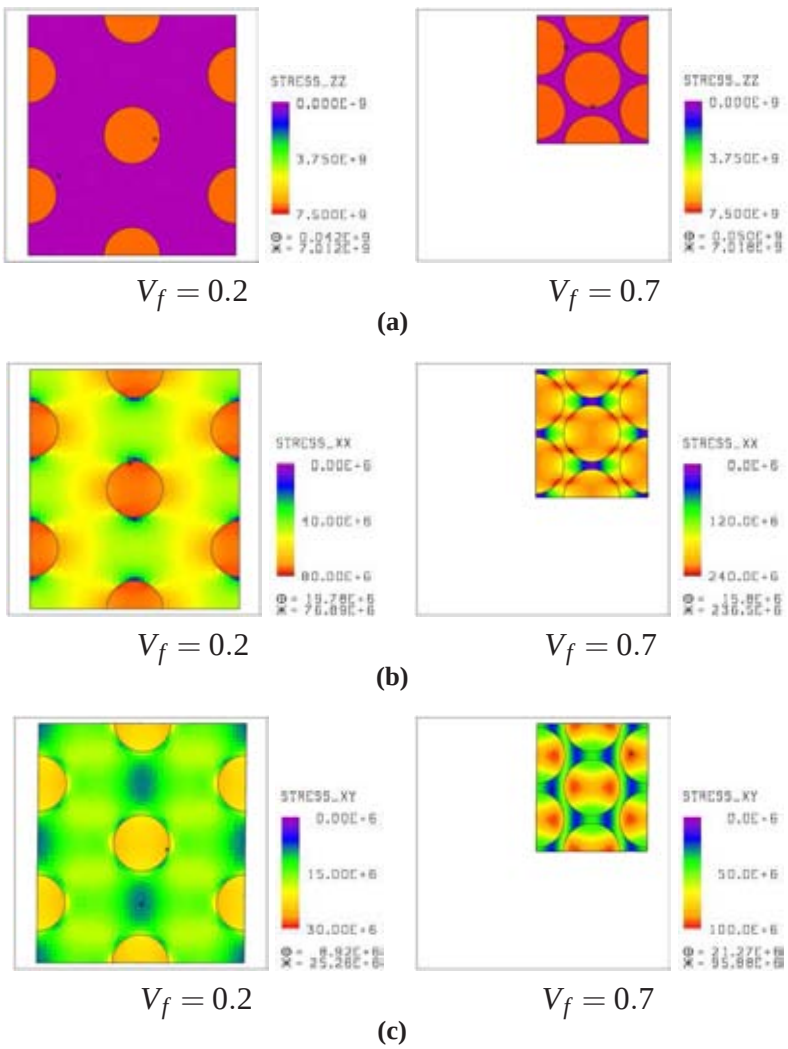

$V_f = 0.2$ $V_f = 0.7$

(a)

$V_f = 0.2$ $V_f = 0.7$

(b)

$V_f = 0.2$ $V_f = 0.7$

(c)

Figure 3.4. Stress distribution contour plots at applied average strains of 1% for fiber volume fractions of 20 and 70% effective fibers, and with the interphase replaced by the matrix: (a) Normal stress σ_{11} due to applied normal strain $\overline{\varepsilon}_{11}$ using a 0-7.5 GPa scale for each V_f; (b) Normal stress σ_{22} due to applied normal strain $\overline{\varepsilon}_{22}$ using scales of 0-80 and 0-240 MPa for $V_f = 0.2$ and 0.7, respectively; (c) Shear stress σ_{23} due to applied shear strain $\overline{\gamma}_{23}$ using scales of 0-30 and 0-100 MPa for $V_f = 0.2$ and 0.7, respectively.

local stress state in and around the effective fiber which results in an increase in the average stress state, and which is also believed to explain the difference between the finite element and composite cylinders solutions for effective elastic properties at high volume fractions.

It can also be noted in Figures 3.4(b) and 3.4(c) that, at high volume fractions, the stress in the fiber is not only augmented, but becomes increasingly non-uniform. This has important consequences for previous modeling efforts like Seidel and Lagoudas (2006a) wherein effective fiber representations of CNTs have been used in conjunction with traditional Mori-Tanaka (Qiu and Weng, 1990) and self-consistent (Hill, 1965) averaging techniques. Unlike the composite cylinders approach, the Mori-Tanaka and self-consistent micromechanics methods make use of the Eshelby tensor (Eshelby, 1957), therefore assuming a uniform stress state in the fibers. Thus, at high fiber volume fractions, use of the Mori-Tanaka or self-consistent techniques for CNT reinforced composites may be increasingly less accurate approaches.

The stresses induced in the hollow fiber FEA representation, although not shown, are much higher than those for the effective fiber FEA representation. This is to be expected due to the higher stiffness of the hollow fiber and the its corresponding smaller volume of load-carrying material. This increased stress in the hollow fiber also results in an increase in the stress state in the surrounding matrix material. However these increases in the stress state are not sufficiently high so as to counteract the contribution of the zero-stress regions of the hollow fibers such that the average stress in the hollow fiber FEA representation is in fact lower than the average stress in the effective fiber FEA representation. Thus, the difference in effective properties observed between the hollow and effective fiber FEA representations at high fiber volume fractions is confirmed to be a result of the effective fiber FEA representation's inability to accurately account for the hollow region. However, for physically obtainable CNT-epoxy composite volume fractions which are less than 10% and certainly much less than 60%, either hollow or effective fiber FEA representations can be used.

While experimental and computational evidence has been obtained for the existence of an interphase region between CNTs and polymer matrices (McCarthy et al., 2002; Odegard et al., 2005), the exact size and material properties of such interphase regions are still an active area of discussion in the research community (Odegard et al., 2005; Wagner, 2002). As such, interphase regions of various sizes and stiffnesses are used in a parametric study in the present work. However, in each case, the interphase regions around the individual fibers of the respective RVEs are taken to be of the same size and stiffness so that the composite consists of identical high-stiffness hollow fibers with identical interphase regions embedded in the matrix.

The inclusion of an interphase region constitutes the introduction of a length parameter, in addition to those length parameters introduced by having hollow fibers and/or clustered arrangements, which for nanocomposites is quite significant as the fiber radius and interphase thickness are of the same order of magnitude. Motivated by the chemistry of the functionalization process (Zhu et al., 2003, 2004), the interphase thickness, once identified, is taken as not varying with changes in fiber size or in hollow fiber thickness. Thus, as fiber volume

fraction is increased for a given RVE, so too is the interphase volume fraction. In addition, the constant thickness of the interphase region produces effective elastic properties which do not necessarily scale with fiber geometry. In contrast, the length parameters introduced as a result of having hollow fibers or due to clustering of fibers could scale with fiber size.

The constant thickness of the interphase with increasing volume fraction also has consequences for the composites cylinders solution in the form of a maximum fiber volume fraction for which the composites cylinders solution can be applied. This maximum fiber volume fraction is determined as a result of the maximum packing fraction based on the interphase outer radius (i.e., where the interphase regions of adjacent fibers come into contact), and can be substantially lower than the maximum fiber packing fraction of 90%. Above the maximum fiber volume fraction for composite cylinders, finite element simulations which can accurately account for the non-cylindrical shapes of the residual matrix and interphase regions can be used.

The results of a parametric study of the effects of interphase regions of various stiffnesses on the effective transverse modulus, E_{22}, for the case of well-dispersed fibers are shown in Figure 3.5 for an interphase thickness of 1.7 nm (i.e., equal to twice the fiber outer radius selected based on Figure 1.1). Interphase stiffnesses of 1/2, 1, 5, and 10 times the stiffness of the matrix (i.e., $E = 1.5$, 3, 15, and 30 GPa with $\nu = 0.3$) are used and the effective transverse modulus is obtained for volume fractions up to the limit volume fraction for the composite cylinders solution (i.e., a volume fraction of 11%). As presented in Figure 3.5, both the finite element simulations and the composite cylinders solution are in excellent agreement and indicate large differences in effective modulus relative to the no-interphase case. In fact, to obtain an equivalent value for the effective transverse modulus as calculated for the 30 GPa interphase at 9% fiber volume fraction, a fiber volume fraction of 60% in the no-interphase case would be required. At that same volume fraction, the 1.5 GPa interphase results in a 44% decrease in the effective transverse modulus. Thus, it is observed that the effective properties associated with the transverse directions can be greatly impacted by the presence of an interphase region, particularly if that interphase region is a compliant interphase and therefore representative of poor load transfer from the matrix to the fiber.

The column identified as PH (i.e., for the perfect hexagonal arrangement) in Figure 3.6 summarizes the results of an additional comparison of the effects of interphase regions on the effective transverse modulus for the well-dispersed case at a specific fiber volume fraction of 10%. For these cases, the interphase thickness is taken to be 0.35 nm (reflective of observations made in Seidel et al. (2005)), resulting in an interphase volume fraction also of 10%. Results for two interphase stiffnesses are provided, a stiff and compliant interphase with stiffnesses of 10 times and $1/10$ the matrix stiffness, respectively, denoted as 10X and 0.1X in the figure. From Figure 3.6, good agreement between finite element representations and the composite cylinders solution is again observed, and direct comparison of the stiff and compliant interphases relative to the no-interphase case can be readily discerned. In this case, the effect of the 0.1X interphase is to lower the effective transverse modulus by 34% relative to the well-dispersed, no-interphase case, whereas the effect of the 10X interphase increases the effective transverse modulus by 15%. Additional results provided

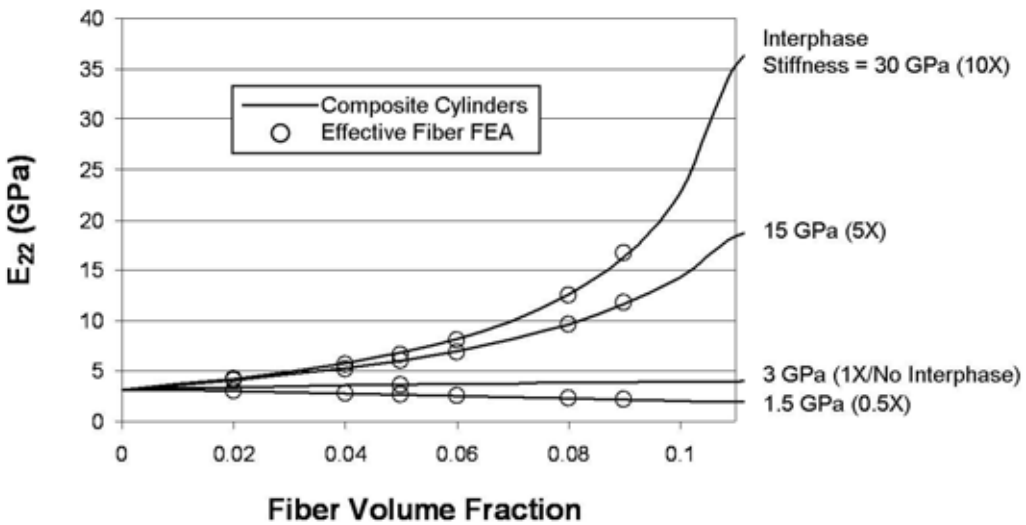

Figure 3.5. Effects of interphase stiffness on the effective transverse modulus, E_{22}, for well-dispersed fibers. Results using three different interphase stiffnesses (1.5, 15, and 30 GPa) are shown along the with previous results with no interphase region. Results are for an interphase thickness of 1.7 nm, or twice the fiber radius, making the limit volume fraction for the composite cylinders solution to be 11%.

in the figure for columns A through E will be discussed in the computational portion of the subsequent chapter on clustered arrangements.

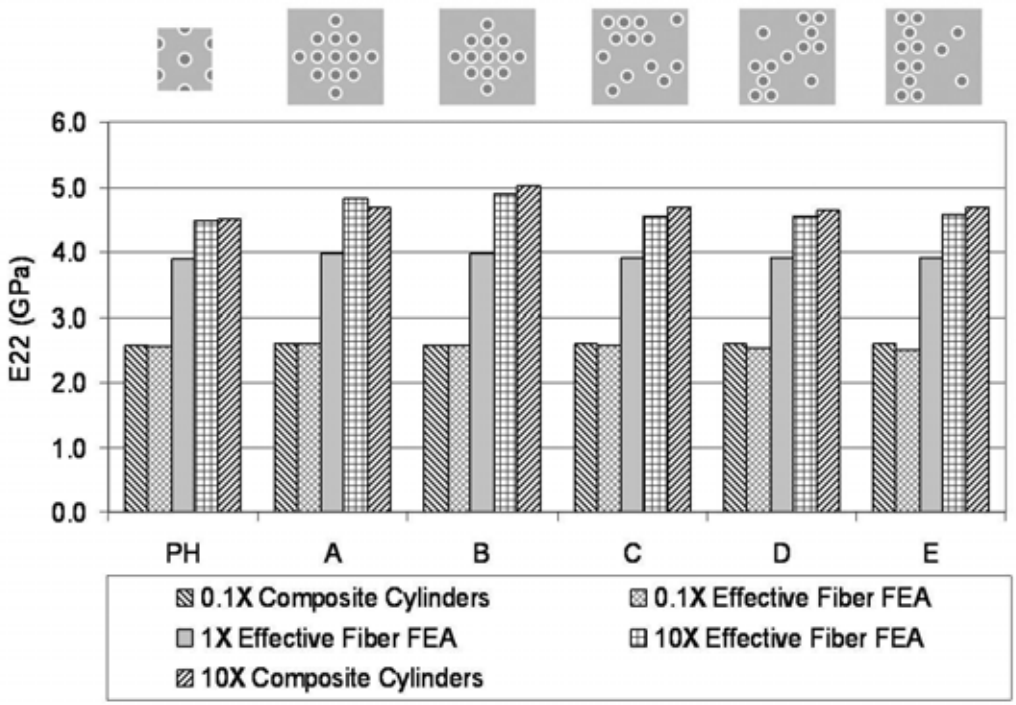

Figure 3.6. Summary of the independent and combined effects of clustering and interphase regions on the effective transverse modulus, E_{22}. Both FEA and composite cylinders results are provided for each case, where for the clustered cases, the composite cylinders method is coupled to the Mori-Tanaka averaging technique. Both the fiber and interphase volume fractions are set at 10% for all cases with interphase stiffnesses 0.1, 1.0 (i.e., no interphase), and 10.0 times that of the matrix. The results in the column denoted PH correspond to well-dispersed fibers, and those in the columns A-E to clustered fiber arrangements, as pictured by the schematics above the result columns.

Chapter 4

Effective Properties of Clustered Carbon Nanotube Reinforced Composites

Analytic Approach for Clustered Carbon Nanotube Reinforced Composites

It has been observed that, due to van der Waals forces, CNTs have a tendency to bundle or cluster together making it quite difficult to produce well dispersed CNT reinforced composites (Cooper et al., 2002; Fisher, 2002). As such, it may be necessary to incorporate the effects of clustering in the prediction of effective elastic properties for the RVE in Figure 2.1(b). A number of research efforts have sought to ascertain the effects of clustering on the effective elastic properties of composites. Ghosh and Moorthy (1995) and Ghosh et al. (1997) used the Voronoi cell finite element method to obtain the stress-strain response for clustered fiber reinforced composites and observed increases in the transverse stress as a result of clustering. Tszeng (1998) studied the elastoplastic response of clusters of spherical particles in metal matrix composites using and equivalent inclusion approach and found no significant effect of clustering on the effective modulus. Boyd and Lloyd (2000) used FEA analysis to study the effects of particle clustering on the fracture toughness in metal matrix composites. Bhattacharryya and Lagoudas (2000) derived a form of the self-consistent model for the effective properties of clustered fiber reinforced composites based on local volume fraction distributions and applied it to bimodal distributions where increases in transverse elastic properties for clustered distributions were found. For aligned short fiber composites, Kataoko and Taya (2000) obtained the effect of clustering on the local stress-strain response, but surprisingly found a decrease in the effective axial stiffness. It should be noted that these previous efforts were more focused on the stress-strain response as opposed to the effective properties, and generally observed the effects of clustering at a single global volume fraction for more traditional composite systems such as carbon fiber reinforced and metal matrix composites. In the present work, the focus is on the effects of clustering on the effective properties of CNT composites using a multi-layered composite cylinder method which is coupled to a multi-phase Mori-Tanaka approach to obtain the effective properties of aligned clustered fiber reinforced composites for a wide range of global volume fractions.

Many research efforts have used tessellation techniques to identify what constitutes a clustered arrangement as well as to delineate different amounts of clustering (Wray et al., 1983; Spitzag et al., 1985; Ghosh et al., 1997; Boselli et al., 1998, 1999; Bhattacharryya and Lagoudas, 2000). Herein, a Dirichlet tessellation is used to account for the degree of clustering by associating with each CNT an amount of surrounding matrix as shown in Figure 4.1. The associated matrix and the CNT are used to obtain an effective CNT-matrix composite via the CC method. These effective CNT-matrix composites are then used to obtain the effective properties of the composite as a whole using the multi-phase Mori-Tanaka method as described by Eqn. 2.3 with P equal to the total number of distinct polygon areas (provided all CNTs are identical and have identical interphase regions) so that the clustered arrangements are treated using the CC/MT method.

For clustered arrangements of aligned CNTs one can readily identify three distinct volume fractions. The first is the global volume fraction, c_g, as expressed in Eqn. (4.1) where N_F is the number of CNTs, A_f is the area of a CNT based solely on its outer radius (all having the same outer radius), and A_T is the total area of composite. This is the volume fraction of the total CNT volume (including the hollow regions) in the matrix relative to the total volume of the composite. Second is the volume fraction of each CNT within its associated matrix expressed in Eqn. (4.2) and referred to as the local volume fraction, c_L. It is the volume fraction directly obtained from the tessellation results with A_i referring to the area of the polygon used to define the amount of associated matrix. The local volume fraction is the volume fraction used in the CC portion of the CC/MT. The third volume fraction is used to denote the overall volume fraction of the effective CNT-matrix composites as obtained from a given local volume fraction, and as such, is referred to as the global-local volume fraction, c_{g_L} as given by Eqn. (4.3), where n_i is the number of times a given local volume fraction occurs as a result of the tessellation. The global-local volume fractions are the volume fractions used in the multi-phase Mori-Tanaka portion of the CC/MT method with the c_{g_L} values equal to the c_l values in Eqn. 2.3 for each distinct local volume fraction up to P distinct local volume fractions.

$$c_g = \left(\frac{N_F A_f}{A_T} \right) \tag{4.1}$$

$$c_L = \left(\frac{A_f}{A_i} \right) \tag{4.2}$$

$$c_{g_L} = \left(\frac{n_i A_i}{A_T} \right)^2 \tag{4.3}$$

The Dirichlet tessellation procedure used to obtain the local volume fractions is a well established geometric technique for obtaining the minimum area polygons encompassing a given set of seed points, which for the present work denotes the set of CNT centers (Wray et al., 1983). The procedure involves the connecting of seed points to all other seed points by a straight line, the perpendicular bisectors of which are constructed and used to identify the polygonal boundaries. Thus, regions in the composite where CNT center density is quite high (clustered regions) will produce small polygons and regions where the

CNT center density is low will produce larger polygons as shown in Figure 4.1. Note that applying the tessellation routine for the hexagonal arrangement of CNTs which represents well dispersed CNT composites would produce identically sized polygons whose local volume fraction would be identically equal to the global volume fraction. This corresponds to having a distribution of local volume fractions represented by the Dirac function and is indicative of the arrangement not being clustered. In contrast, if there are significant numbers of both small and large polygons, then a bimodal distribution in polygon size will occur indicating the existence of bimodal clustering in the composite.

Having completed the tessellation procedure, the local volume fractions are obtained. In order to take advantage of the CC method in finding effective CNT-matrix composite properties, the polygons encompassing the CNTs are converted into concentric rings of associated matrix. To do this, each polygonal area is calculated and set equal to the area of a circle of unknown radius. The area equivalence is used to determine the radius of the circle, and the circle is set to be concentric with the CNT which it encompasses, thus maintaining the local volume fraction distribution. This process is depicted graphically in Figure 4.1. The assumption that the polygons obtained from the Voronoi tessellation can be replaced by equivalent circles has been studied using FEA. Indications were that the average concentration factors are not much affected, however for fibers in very close proximity, elevated stress states do cause FEA predictions of effective properties to be above those obtained by the approach applied herein. It should be noted that in the present work, all the CNTs are the same size and as such, polygons of the same area (but perhaps different shape) will produce identical local volume fractions. It should also be noted that for the subsequent Mori-Tanaka method, some small volume fraction of associated matrix from each polygon is set aside as the matrix in which the effective CNT-matrix composites are embedded, i.e. such that c_m in Eqn. 2.3 is nonzero.

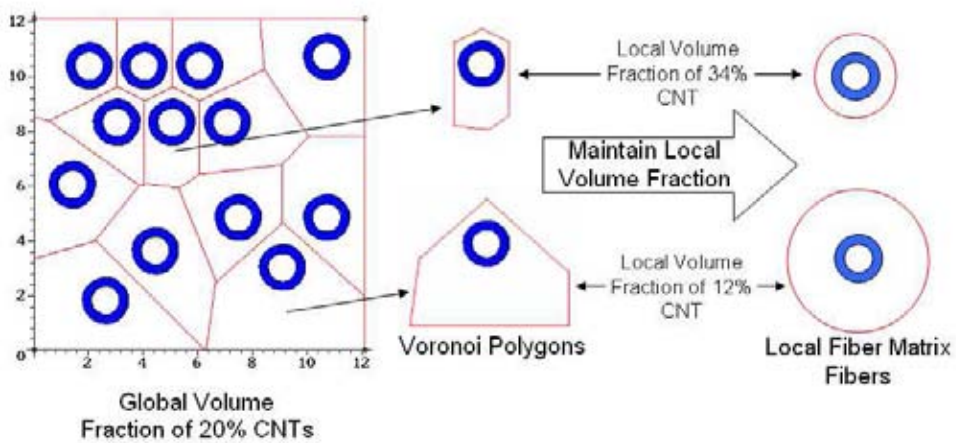

Figure 4.1. Conversion of tessellated polygon to concentric circle of associated matrix for use in the CC/MT method to account for clustering.

The CC method is applied P times to obtain effective CNT-matrix composite properties where P denotes the number of distinct local volume fractions. In each application of the CC method, N is greater than or equal to two, with the first layer corresponding to the CNT and the N^{th} to the associated matrix, thus allowing for the presence of interphase regions. The P CNT-matrix composites are then embedded in the remaining matrix at the appropriate global-local volume fractions corresponding to the number of polygons of a given identical size, and the multi-phase Mori-Tanaka method is applied.

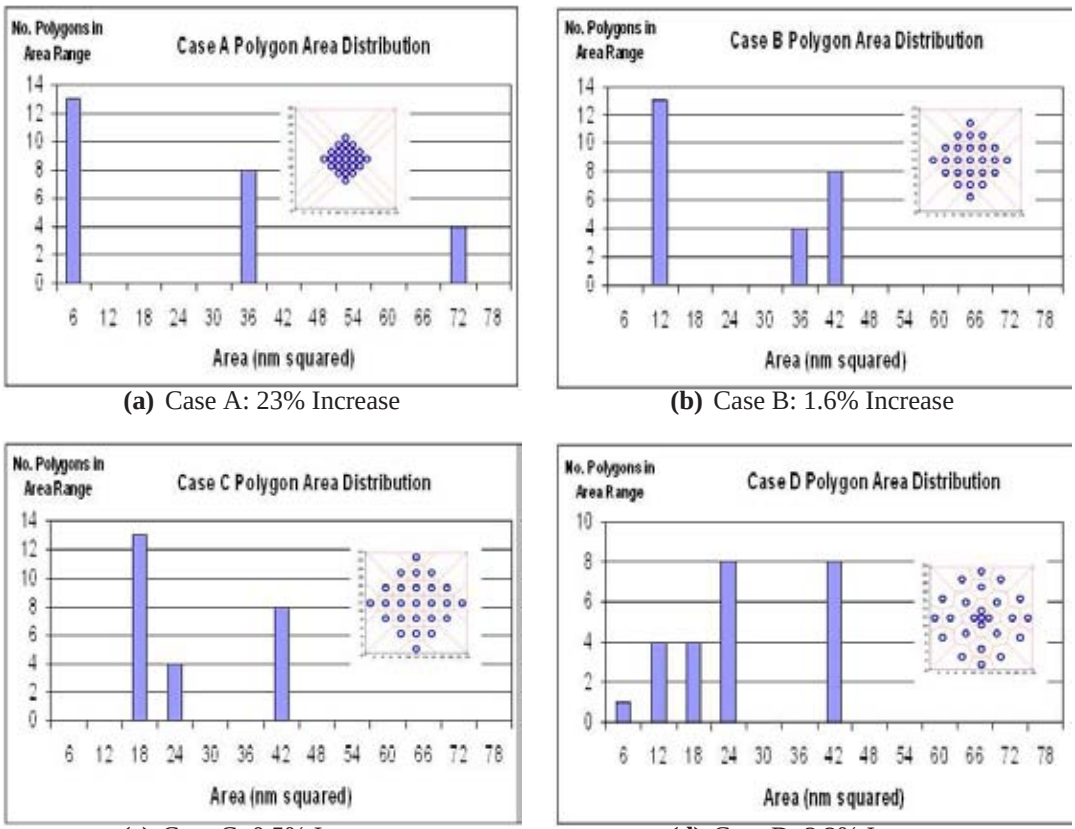

(a) Case A: 23% Increase

(b) Case B: 1.6% Increase

(c) Case C: 0.5% Increase

(d) Case D: 2.2% Increase

Figure 4.2. Polygonal area distributions for four clustered cases at 10% global volume fraction using 25 CNTs. Insets denote the CNT arrangements studied. Percent differences relative to the well dispersed CNT distribution value of E_{22} are also provided.

This technique has been applied to several test cases involving a range from thirteen to twenty-five identical CNTs in the absence of interphase effects embedded in the polymer matrix, i.e. for maximum values of P ranging from thirteen to twenty-five and in all P cases, N equal to two. Here the CNTs were arranged within the matrix in such manner so as to introduce clustering. As would be expected, it was observed that the clustered composite's axial Young's modulus was unaffected by clustering, and as such, only the transverse Young's modulus results are provided (recall that the other effective properties

follow the same trend as E_{22} and thus are not reported). Figure 4.2 provides the tessellation results of four test cases at 10% global volume fraction of effective CNTs for four fiber arrangements shown as insets in Figure 4.2 where the distributions in polygonal areas are provided to give some insight as to the degree of clustering obtained in each case. Clearly the distributions indicate that Case A constitutes the most clustered case represented as the distribution is spread over the largest range, i.e. deviates the most from the well dispersed distribution. From Case B to C the degree of clustering steadily decreases as indicated by the decreasing range of polygonal areas. Thus, indeed the most clustered case, Case A, deviated the most from the well dispersed CNT value for effective transverse modulus by a percent difference of 23%, with Cases B and C exhibiting sequentially less deviation from the well dispersed CNT solution, 1.6% and 0.5%, respectively. Note that the increase in transverse stiffness is consistent with the observations of Ghosh and Moorthy (1995) and Ghosh et al. (1997) which indicated an increased stress state as a result of clustering, thereby increasing the average stress which is used in obtaining effective properties.

Figure 4.3 provides the effects of clustering on the effective transverse Young's modulus for a range of global volume fractions for a single cluster arrangement in terms of percent difference relative to the well dispersed CNT effective transverse modulus at each volume fraction. In Figure 4.3 it is observed that, in general, there is an increasing effect of clustering on the deviation from the well dispersed CNT effective transverse modulus with increasing global volume fraction from 0-40% (0% corresponding to pure matrix and therefore clearly no effect of clustering). However, the effect of clustering reaches a maximum and then begins to drop sharply as a global volume fraction of 90% is approached (recall that 90% is the maximum packing fraction for aligned fibers and therefore can not be clustered). Thus, it is observed that the effect of clustering is to increase in magnitude only the transverse to CNT alignment properties of the transversely isotropic effective composite as compared to the well dispersed CNT composite's effective elastic properties, and that this augmentation in transverse elastic properties is initially increasing with increasing global volume fraction of CNTs before returning to having no effect at the maximum packing fraction.

As previously stated, the effective CNT-matrix composites were re-embedded in the small amount of matrix which was set aside from each polygon. Figure 4.4 provides the results of a parametric study on the effects of increasing the amount of matrix set aside from each polygon on the effective transverse modulus of clustered composites. For the cases considered, it is observed that the effect of setting aside increasing amounts of matrix is to increase the deviation of the clustered solution from the random distribution results only slightly. It should be noted that the self-consistent method could readily be used in place of the Mori-Tanaka method in determining the effective properties of clustered CNT arrangements. As can be seen in Eqn. 2.1, the self-consistent method does not require any amount of matrix to be set aside for the effective CNT-matrix composites to be embedded in as the fibers are instead embedded in the effective medium. However, the Mori-Tanaka method was utilized here as a result of the good agreement with the FEA results previously observed. The CC method is also in good agreement with FEA results, but is only capable of considering one composite cylinder assemblage at a time, i.e. a single CNT and its

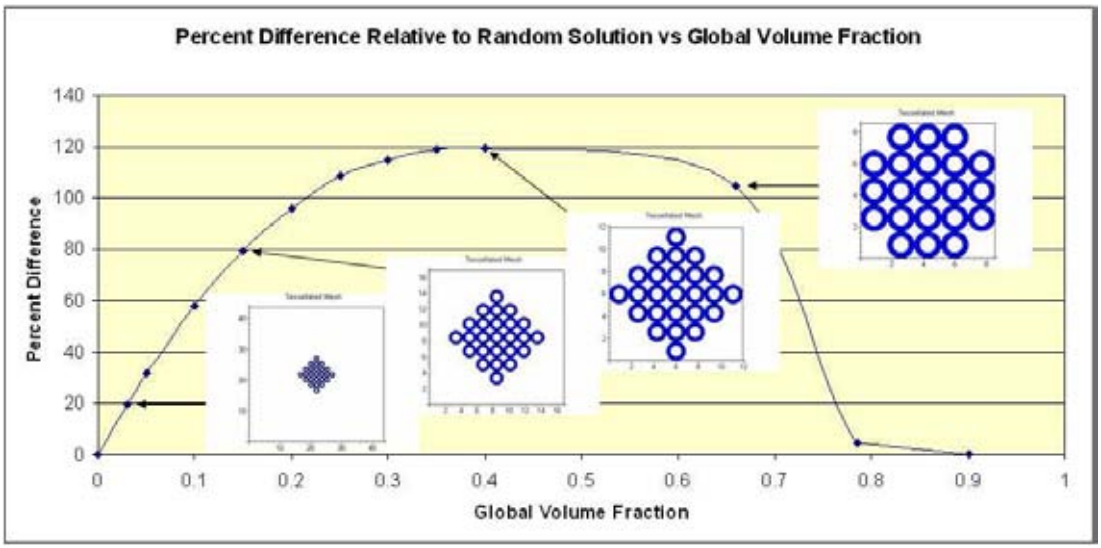

Figure 4.3. Effects of clustering on the transverse moduli, E_{22}, at various global volume fractions in terms of percent difference relative to well dispersed CNT results.

(N-1) surrounding layers, and would not be able to address the differences in local volume fraction associated with each CNT in clustered arrangements.

Computational Approach for Clustered Carbon Nanotube Reinforced Composites

The resulting effects of clustering of high-stiffness hollow fibers with and without interphase regions on the effective elastic properties of aligned, hollow fiber composites are studied in this section using both analytic and computational micromechanics approaches. For the clustered arrangements of fibers, the computational representative volume elements, like the one denoted by the dashed lines in Figure 3.1(b), contain several dispersed fibers, some of which are in closer proximity than others. Additional clustered arrangements studied are identified at the tops of columns A through E in Figure 3.6, all consisting of deviations from the perfect hexagonal array. As was previously noted for the well-dispersed case atop the column identified as PH, the results reported in the present work are for clustered arrangements having fiber and interphase volume fractions of 10%, with the interphase regions having stiffnesses of either 0.1, 1, or 10 times that of the matrix, with the 1X cases being indicative of clustered arrangements with no interphase regions.

There are many different possible arrangements of fibers in an RVE that can be used to

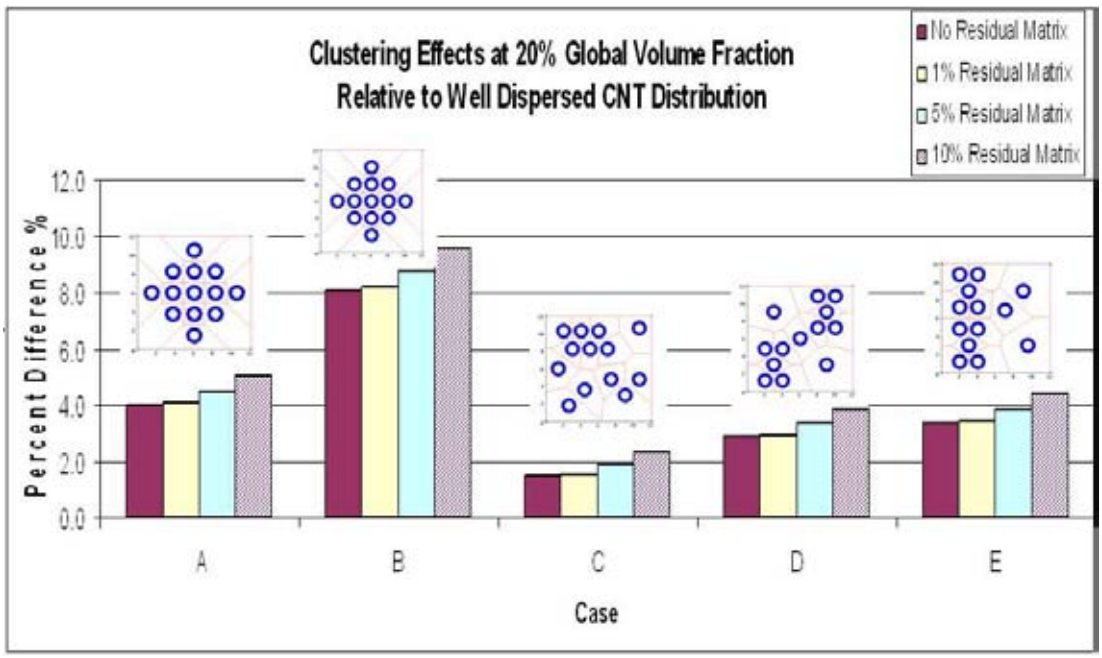

Figure 4.4. Parametric study on how the amount of matrix set aside from each polygon effects the clustered solutions for effective transverse modulus using the CC/MT method.

represent clustering, of which those chosen for the present work are only a small subset. Nevertheless, it is felt that the present results will be representative of the general effects that arise from high-stiffness hollow fiber clustering and therefore relevant to CNT reinforced composites. It should also be noted that any deviation from the perfect hexagonal arrangement could result in effective properties which are not transversely isotropic. As such, it is necessary to perform all six numerical simulations previously discussed to determine the complete set of effective orthotropic engineering elastic constants. Due in large part to the periodic boundary conditions applied, the effective properties of the clustered arrangements studied herein remain very nearly transversely isotropic.

In obtaining the effective elastic properties for the clustered arrangements via FEA, the same periodic boundary condition sets are used on the clustered RVEs to obtain volume averaged stress for a given applied strain. The finite element results are compared to analytic micromechanics results obtained using a combination of the composite cylinders approach with the Mori-Tanaka method as discussed in detail in previous work by Seidel and Lagoudas (2006a). In this approach, a Dirichlet tessellation procedure is used to identify local volume fractions for each fiber. The local volume fractions are used to associate with each fiber a corresponding portion of the matrix. The effective properties of these local fiber-matrix assemblages are then determined using a composite cylinders solution. The number of fibers each having a given local volume fraction constitutes a separate ef-

fective phase, and the overall effective properties of the clustered composite as a whole are determined by using these effective phases in conjunction with the Mori-Tanaka approach. Recall that the length parameters introduced as a result of clustering or of hollow fiber thickness scale with fiber size. However, the inclusion of an interphase region of constant thickness introduces a length parameter which does not scale with fiber size into both well-dispersed and clustered arrangements, so that the differences between the 10X and 0.1X cases and the 1X cases in Figure 3.6 can be attributed to the length parameter associated with the interphase thickness. A summary of the effects of clustering and interphase regions on the other effective engineering moduli is provided in Table 4.1, where it is observed that the effective axial modulus is not affected by the clustering in the transverse plane.

Table 4.1. Summary of the combined and independent effects of clustering and interphase regions on the effective engineering properties for composites with 10% fiber and 10% interphase region volume fractions. The average effect is the is the average percent difference of the studied cases PH, A, B, C, D, and E relative to the 1X PH case (i.e., the well-dispersed, no-interphase case). The effect variation with clustering is the difference between the highest and lowest percentage changes also relative to the 1X PH case.

Property	0.1X interphase		1X (no interphase)	10X interphase	
	Average Effect (%)	Variation with Clustering (%)	Variation with Clustering (%)	Average Effect (%)	Variation with Clustering (%)
E_{11}	-0.48	0.10	0.10	3.75	0.10
E_{22}	-34.36	2.24	2.33	19.49	10.35
ν_{12}	3.74	0.79	0.96	-0.53	1.87
ν_{23}	-6.42	5.06	3.17	-7.01	11.63
G_{12}	-34.35	1.97	1.96	19.95	7.78
G_{23}	-36.20	2.95	2.24	14.20	8.38

The effects of clustering without the effects of an interphase region on the effective transverse modulus can be assessed by comparing the 1X well-dispersed result in the PH column with the 1X results in columns A through E in Figure 3.6. Such a comparison demonstrates that there is hardly any difference in the effective transverse modulus relative to the well-dispersed solution for the clustered arrangements considered. Case B, which is identified as the most clustered arrangement as measured by the distribution of local volume fractions obtained via Dirichlet tessellation, shows a slightly larger increase in effective transverse modulus relative to the well-dispersed case than do the other clustering cases. However, all demonstrate small increases in effective transverse modulus on the order of 3% or less.

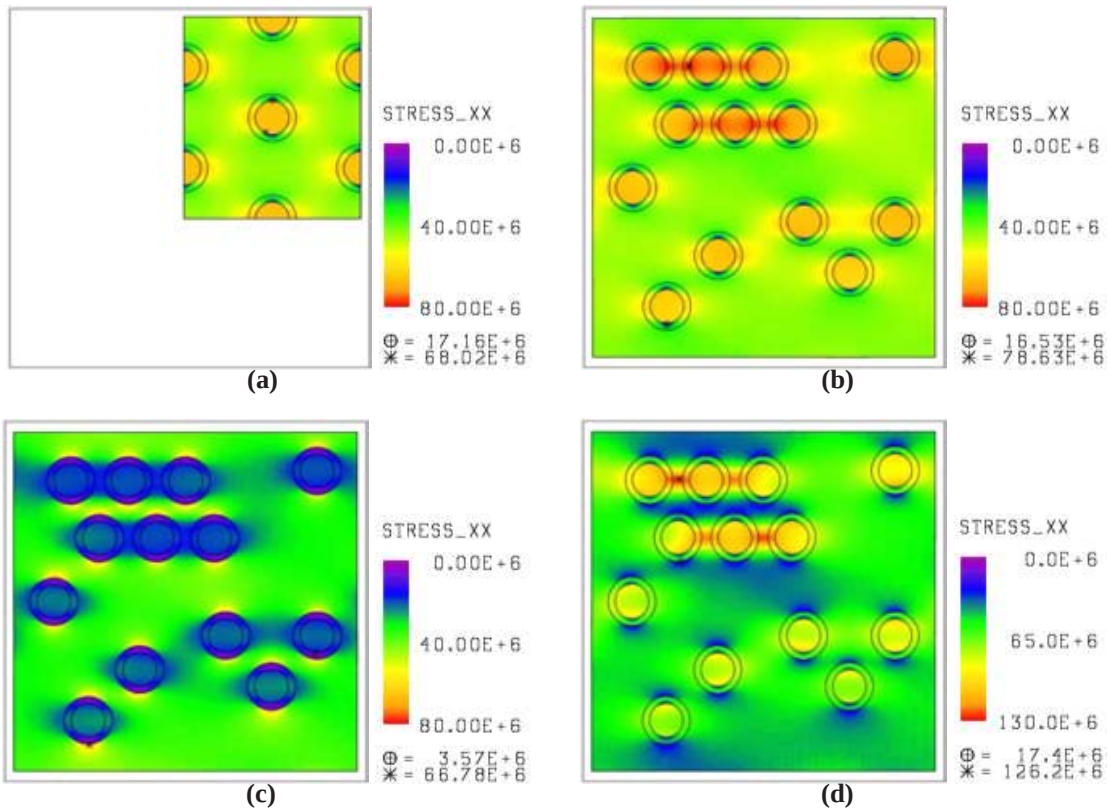

Figure 4.5. Stress distribution contour plots of the resulting normal stress σ_{22} from an applied average strain $\overline{\varepsilon}_{22}$ of 1% for 10% fiber and interphase volume fractions and for various interphase stiffnesses: (a) 1X PH well-dispersed arrangement (0-80 MPa scale); (b) 1X Case C clustered arrangement (0-80 MPa scale); (c) 0.1X Case C clustered arrangement (0-80 MPa scale); (d) 10X Case C clustered arrangment (0-130 MPa scale).

The increase in effective transverse modulus as a result of the clustering effect observed in the 1X cases of Figure 3.6 can be explained by examining Figures 4.5(a) and 4.5(b), which provide the σ_{22} stress distribution contour plots for the well-dispersed and clustered Case C 1X interphase cases at 10% fiber volume fraction for an applied average transverse strain, $\overline{\varepsilon}_{22}$, of 1%. The fibers in the cluster of fibers in the upper left corner of Figure 4.5(b) demonstrate an increased stress state in the fibers and surrounding matrix relative to the fibers in the well-dispersed case as a result of the interactions between effective fibers in close proximity. However, this localized increase in the stress state results in a peak stress value of 78 MPa, only 10 MPa larger than the peak stress in the well-dispersed 1X case, and hence, only a marginal increase in the effective transverse modulus.

The combined effects of including clustering and interphase regions on the effective transverse modulus, E_{22}, are also presented in Figure 3.6, denoted by the 10X and 0.1X la-

bels in columns A through E. For comparison purposes both the finite element and the coupled composite cylinders/Mori Tanaka method previously discussed are shown. From Figure 3.6, it is observed that the combined effects of clustering and interphase regions differ overall depending on the interphase stiffness. For the 0.1X well-dispersed (PH) and clustered cases (A-E), a uniform decrease in the effective transverse modulus of approximately 33-36% relative to the 1X well-dispersed case is observed. This indicates that the composite is interphase dominated in that, regardless of the degree of clustering, it is the interphase regions which are the main contributor to the reduction in effective transverse modulus. For the 10X well-dispersed and clustered cases, the increase in transverse modulus ranges from 15% for the well-dispersed case up to 25% for the most clustered case, Case B. Thus, for the 10X cases, there is a measurable interaction between clustering and interphase effects which causes larger increases in the effective transverse modulus than either effect independently.

Reasons for the different trends in the effective transverse modulus results observed between the 0.1X and 10X clustered arrangements can again be better understood by examining the σ_{22} stress contour plots provided in Figures4.5(c) and 4.5(d) for the 0.1X and 10X cases, respectively. In Figure 4.5(c), the compliant nature of the interphase results in almost no stress being transferred to the fiber, which explains why clustering has relatively little effect on the effective transverse modulus for the compliant interphase cases. Figure 4.5(d), however, shows that the stiff interphase leads to large increases in stress in the fibers and in the matrix as compared to both the well-dispersed and clustered, no-interphase cases. These elevated stresses, which are especially large for fibers in close proximity, in turn lead to significant increases in the effective transverse modulus. These strong interactions among clustered fibers produce a peak stress in the 10X clustered case shown which is 60% larger than the peak stress in the 1X clustered case, resulting in the noted coupling between interphase and clustering effects (note the different scale bar for Figure 4.5(d)). This again points to the large impact that the interphase regions can have on the effective properties associated with the transverse direction in representing various degrees of load transfer.

Additional detailed explicit results for the effective engineering elastic constants other than the effective transverse stiffness are not given here. Rather, Table 4.1 provides an overview of the results with the "Average Effect" column giving the nominal magnitude of the interphase effect for the studied well-dispersed and clustered arrangements and with the "Variation with Clustering" column stating how much variation with clustering arrangement there is for each property (E_{11}, E_{22}, ν_{12}, ν_{23}, G_{12}, and G_{23}). For example, for the 0.1X interphase stiffness, the effect of including the interphase region on G_{12} is large (approximately a 34% decrease), but nearly the same magnitude for all CNT arrangements (less than 2% variation). Consistent with the observations made for the effective transverse modulus, it is observed in general that for the compliant interphase regions, there is less variation in the effective engineering properties with clustering than for the stiff interphase regions with clustering.

Chapter 5

Effective Properties for Carbon Nanotube Reinforced Composites with Randomly Oriented Nanotubes

The effective properties of composites with randomly oriented non-clustered CNTs, such as in Figure 2.1(a) but where CNTs are not clustered into bundles, were studied and compared to aligned non-clustered results. For both randomly oriented and aligned results, the CC/MT method is applied, with random orientation being accounted for by considering each separate orientation of a given CNT as an additional phase in the multi-phase Mori-Tanaka portion of the CC/MT and integrating over all possible orientations as discussed by Entchev and Lagoudas (2002). The resulting effective properties for the randomly oriented CNT composite are isotropic, despite the CNTs having transversely isotropic effective properties. To isolate the effects of random orientation, identical CNTs with no interphase regions were considered. Table 5.1 summarizes the input parameters and Table 5.2 the effective properties obtained from the randomly oriented CNT composites using the CC/MT method.

Table 5.1. Randomly Oriented Mori-Tanaka Input Data.

Matrix: EPON 862	
$E = 2.026$ GPa (Zhu et al., 2004; Yang et al., 2004)	$\nu = 0.3$
Effective Carbon Nanotubes	
$E_{11} = 704$ GPa	$\nu_{12} = 0.14$
$E_{22} = 345$ GPa	$\nu_{23} = 0.3764$
$\mu_{12} = 227$ GPa	

Also in Table 5.2 are provided experimentally obtained data by Schadler et al. (1998), who tested composites of this type with 5% wt CNTs, and by Zhu et al. (2004) and Yang et al. (2004) who have manufactured and tested a wide range of functionalized and unfunction-

alized CNT reinforced composites. As seen in Table 5.2 and graphically demonstrated in Figure 5.1, the Mori-Tanaka method results at low volume fractions compare well with the effective properties of the experimentally tested epoxy composites. Higher volume fraction comparisons are not presently possible as currently it is difficult to make epoxy composites with volume fractions of CNTs much higher than 10% due to the large increase in viscosity of the liquid polymer with the introduction of CNTs. This point is emphasized if one considers the ideal case of having well-dispersed and well-aligned CNTs in a matrix material. At 1% volume fraction, CNTs would have an average center-to-center separation of 17nm while at 10% volume fraction, the center-to-center separation would be 5.4nm (based on tessellation and polygon to sphere conversion of the regular hexagonal array of CNTs). For the cross-linked thermoset epoxy matrix used in the present study, such a small spacing may be the source of the large viscosity increases, as for noncross-linked systems, such as polystyrene, CNT volume fractions of up to 50% have been obtained (Watts et al., 2003), though mechanical properties were not the focus. It should be noted that in general the Mori-Tanaka method will not produce different results for tension and compression moduli; that the Mori-Tanaka results compare more favorably with Schadler's compression results is more likely attributed to better load transfer to the CNTs in compression versus tension. Recall that the micromechanics techniques discussed herein all presume perfect adhesion between the CNTs and the matrix. However, experimental evidence indicates that this is too strong of an assumption (Schadler et al., 1998), and indeed, there is currently much research devoted specifically to improving the adhesion between the two through functionalization(Namilae et al., 2004).

Table 5.2. Randomly Oriented Mori-Tanaka Results and Comparison to Experimental Data.

Experimental Case	**Experimental Modulus**	**Mori-Tanaka Modulus**
Barrera Functionalized 1 at 0.5% Volume Fraction	2.632 GPa	2.6293 GPa
Barrera Functionalized 2 at 0.5% Volume Fraction	2.650 GPa	2.6293 GPa
Barrera Functionalized 2 at 2.0% Volume Fraction	3.400 GPa	4.4340 GPa
Schadler in Tension at 2.5% Volume Fraction	3.710 GPa	5.0350 GPa
Schadler in Compression at 2.5% Volume Fraction	5.400 GPa	5.0350 GPa

The axial and transverse effective moduli for composites with randomly oriented CNTs are provided in Figure 5.2 (plotted simultaneously with the aligned CNT results) for the complete range of volume fractions. As can be seen in Figure 5.2(a), without fiber alignment, one can not as readily take advantage of the high modulus of the CNTs. With random orientation, the effective properties become isotropic, and no longer display CNT dominated behavior in any one direction as was the case for the axial direction in aligned composites.

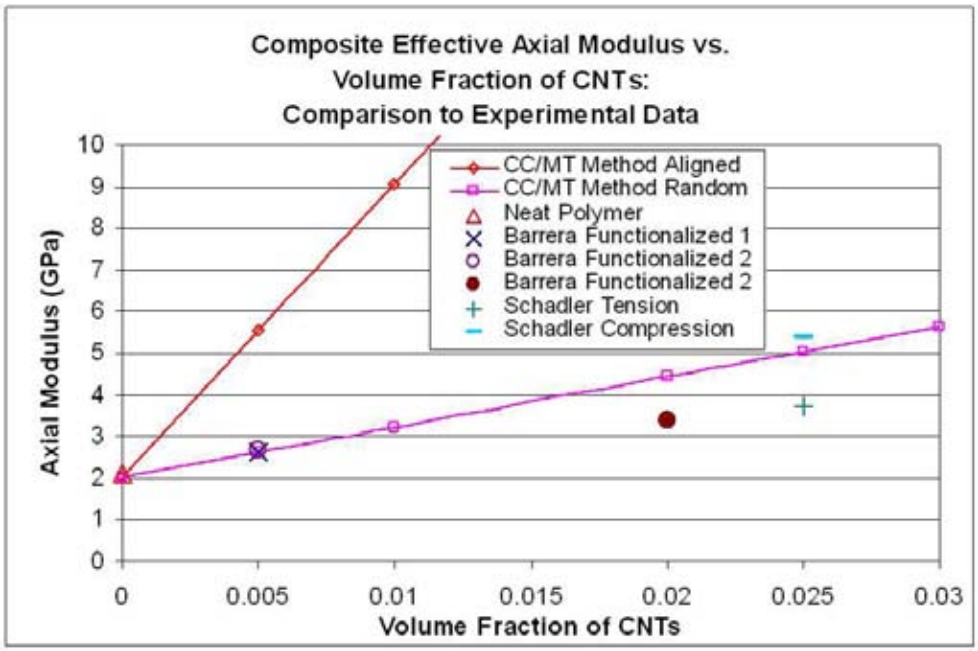

Figure 5.1. Comparison of the axial modulus values obtained using the CC/MT for both aligned and randomly oriented CNT composites to experimentally obtained composite values.

Figure 5.2(b) indicates that, especially at low volume fractions, the isotropic properties obtained are far superior to those obtained in the aligned CNT composites in the direction transverse to the CNTs, and are thus less matrix dominated. As in general it is often desired to increase the stiffness only in the load-bearing directions of a composite, certainly aligned CNT reinforcement would be preferred.

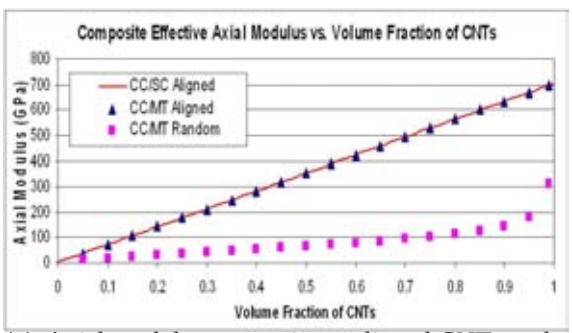

(a) Axial modulus comparison: aligned CNT results indicate CNT dominance of effective properties

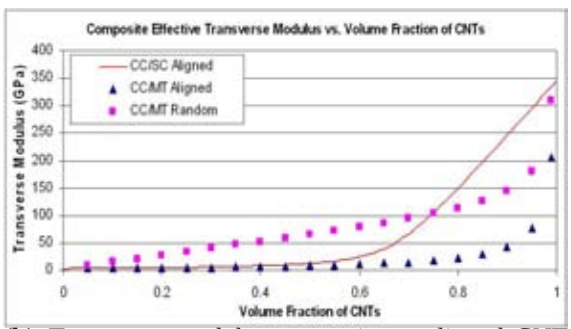

(b) Transverse modulus comparison: aligned CNT results indicate matrix dominance of effective properties

Figure 5.2. Comparison of randomly oriented CC/MT results to aligned CNT CC/MT and CC/SC results. Randomly oriented results indicate isotropic behavior as both axial and transverse modulus results are identical

Chapter 6

Conclusions

The interest in developing and modeling macroscale composites reinforced with CNTs has lead to the use of micromechanics techniques to model the microstructure of composites in which they are employed. Herein a composite cylinders method has been used to convert hollow CNTs into solid effective CNTs using the elastic properties of graphene sheets. Effective CNTs have then been used in the self-consistent and Mori-Tanaka micromechanics techniques, and indicate that, for aligned CNTs composites, the axial Young's modulus is CNT dominated, while all properties associated with the transverse to CNT directions are matrix dominated. FEA results were found to be in good agreement with two of the three analytic solutions obtained. The effects of an interphase on the effective properties of CNT reinforced composites were studied and observed to greatly impact the transverse properties at low volume fractions. An effort was made to incorporate the effects of clustering into the micromechanics modeling from which it was observed the effect of clustering was to augment the effective properties associated with the transverse to CNT alignment directions. Randomly oriented CNT results obtained using the Mori-Tanaka method were found to compare well with results experimentally obtained by Schadler et al. (1998) and Zhu et al. (2004) and Yang et al. (2004). The isotropic properties of composites with randomly oriented CNTs are influenced by CNTs at all volume fractions, but are not CNT dominated in any direction. In light of recently available data using Raman spectroscopy (Hadjiev et al., 2006), future work will include the influence of partial debonding between phases in tension versus compression comparisons.

In order to gain a practical understanding of continuum level mechanical behavior of carbon nanotube composites, computational micromechanics modeling has been used to determine the effective properties of such material systems. Finite element simulations of well-dispersed and clustered arrangements of aligned high-stiffness hollow fibers reflective of continuum representations of carbon nanotube reinforced composites, with and without interphase regions, have been studied and compared to some available analytic micromechanics solutions. The finite element and analytic micromechanics results have been found to be in good agreement for well-dispersed fibers with and without interphase regions for a large range of volume fractions.

The effects of clustering alone on the effective elastic constants were found to be relatively small; an increase in most properties of approximately 2-3% at a fiber volume fraction of 10%, increase in the ν_{12} Poisson's ratio of 1%, and essentially no effect on the axial

modulus, E_{11}. On the other hand, the effects of adding interphase regions alone on the well-dispersed fiber arrangement were typically much more significant: as much as a 15% increase for stiff interphase cases and a 30% decrease for compliant interphase cases. In summarizing these results, it is important to note that the inclusion of an interphase region which has dimensions of nanometers introduces a length parameter unique to nanocomposites in both well-dispersed and clustered arrangements.

The combined effects of clustering and interphase regions were also studied. For the case of compliant interphase regions, all of the effective elastic constants except the axial modulus were found to have changes dominated by the inclusion of the interphase region as the variation with clustering was approximately 5% or less. For interphase regions stiffer than the polymer matrix, the interphase and clustering effects coupled to increase the effective moduli by more than either effect independently. That is, without an interphase region, most effective moduli changed by approximately 3% or less as the clustering arrangement was varied for a fiber volume fraction of 10%, but including the stiff interphase region led to some of the engineering constants differing by 10% or more depending on the clustering arrangement.

Finally, comparisons were made between computational and analytic micromechanics methods, with the key observation being that below 60% fiber volume fraction, excellent agreement between the two methods for all effective elastic constants is obtained. It should be noted that both methods make different assumptions regarding the fiber/matrix and fiber/fiber interactions as exemplified by each method's corresponding RVE, e.g., a perfect hexagonal array for the well dispersed case in the computational micromechanics approach versus a single concentric cylinder RVE in the analytic micromechanics approach. It is also worth noting that there are distinct advantages to both the computational and analytic micromechanics approaches employed herein. The multi-layered composite cylinders analytic micromechanics method is advantageous for well-dispersed arrangements of aligned fiber composites. Provided that each fiber has the same interphase or sequence of multiple interphases, the multi-layered composite cylinders method provides accurate representations for obtaining the effective elastic constants for a continuous range of volume fractions below the critical volume fraction.

Near and above the critical volume fraction, the fiber/matrix interactions become sufficiently complicated that finite element solutions are more advantageous. For example, above the critical volume fraction, there is residual matrix remaining in the composite, but it is no longer concentric to the fiber thereby making its inclusion in a composite cylinders method untenable. Provided the meshing difficulties as phase boundaries become small and complex can be adequately addressed, the computational micromechanics solutions obtained from finite element simulations are best suited near or above the critical volume fraction.

The computational micromechanics approaches have an additional advantage in determining the effective properties for clustered arrangements with little added complexity as compared to the well-dispersed case. For clustered arrangements, the finite element method can better represent the full geometry of the clustered arrangement and directly determine

the effective properties. In contrast, the present analytic approaches can only represent the clustered geometry in terms of local volume fraction in a two stage approach, and subsequently have difficulty retaining important fiber/fiber directional and proximity information which affect the local stress state.

Lastly, certain effective properties are more conveniently obtained using either the analytic or computational micromechanics approach may be more direct. For example, the transverse modulus, E_{22}, is a property which is directly obtained from the six tests in the finite element approach, but is calculated from the other five properties in a composite cylinders approach. Conversely, the in-plane bulk modulus, κ_{23}, can be directly obtained in the composite cylinders approach, but is calculated from the other five engineering properties in the finite element approach.

Overall, both analytic and computational micromechanics methods have their advantages and should be considered for use as needed, using the above guidelines, for high-stiffness hollow fiber composites such as CNT reinforced polymers.

References

Achenbach, J., Zhu, H., 1990. Effect of interphases on micro and macromechanical behavior of hexagonal-array fiber composites. ASME Journal of Applied Mechanics 57, 956–963.

Anifantis, N., Kakavas, P., Papanicolaou, G., 1997. Thermal stress concentration due to imperfect adhesion in fiber-reinforced composites. Composites Science and Technology 57, 687–696.

Benveniste, Y., 1987. A new approach to the application of mori-tanaka's theory in composite materials. Mechanics of Materials 6, 147–157.

Benveniste, Y., Dvorak, G., Chen, T., 1989. Stress fields in composites with coated inclusions. Mechanics of Materials 7 (6), 305–317.

Benveniste, Y., Dvorak, G., Chen, T., 1991. On effective properties of composites with coated cylindrically orthotropic fibers. Mechanics of Materials 12, 289–297.

Benveniste, Y., Miloh, T., 2001. Imperfect soft and stiff interfaces in two-dimensional elasticity. Mechanics of Materials 33, 309–323.

Bhattacharryya, A., Lagoudas, D. C., 2000. Effective elastic moduli of two-phase transversely isotropic composites with aligned clustered fibers. Acta Mechanica 145, 65–93.

Boselli, J., Pitcher, P., Gregson, P., Sinclair, I., 1998. Quantittative assessment of particle distribution effects on short crack growth in sicp reinforced al-alloys. Scripta Materialia 38, 839–844.

Boselli, J., Pitcher, P. D., Gregson, P. J., Sinclair, I., 1999. Secondary phase distribution analysis via finite body tessllation. Journal of Microscopy 195 (2), 104–112.

Boyd, J., Lloyd, D., 2000. Clustering in particulate mmcs. Comprehensive Composite Materials 3, 139–148.

Budiansky, B., 1965. On the elastic moduli of some heterogeneous materials. Journal of Mechanics and Physics of Solids 13, 223–227.

Christensen, R., Lo, K., 1979. Solutions for effective shear properties in three phase sphere and cylinder models. Journal of the Mechanics and Physics of Solids 27, 315–330.

Christensen, R. M., 1979. Mechanics of Composite Materials. Krieger Publishing Company, Malabar, FL.

Cooper, C. A., Ravich, D., Lips, D., Mayer, J., Wagner, H., 2002. Distribution and alignment of carbon nanotubes and nanofibrils in a polymer matrix. Composites Science and Technology 62, 1105–1112.

Dasgupta, A., Bhandarkar, S., 1992. A generalized self-consistent mori-tanaka scheme for fiber-composites with multiple interphases. Mechanics of Materials 14, 67–82.

Dvorak, G., Teply, J., 1985. Plasticity Today: Modeling, Methods and Applications. Elsevier, London.

Entchev, P., Lagoudas, D., 2002. Modeling porous shape memory alloys using micromechanical averaging techniques. Mechanics of Materials 34, 1–24.

Eshelby, J., 1957. The determination of the elastic field of an ellipsoidal inclusion, and related problems. Proceedings of the Royal Society of London 241 (1226), 376–396.

Eshelby, J., 1959. The elastic field outside an ellipsoidal inclusion. Proceedings of the Royal Society of London 252 (1271), 561–569.

Fisher, F., Bradshaw, R., Brinson, L., 2003. Fiber waviness in nanotube-reinforced polymer composites - i: modulus predictions using effective nanotube properties. Composites Science and Technology 63, 1689–1703.

Fisher, F., Brinson, L., 2001. Viscoelastic interphases in polymer-matrix composites: theoretical models and finite element analysis. Composites Science and Technology 61, 731–748.

Fisher, F. T., 2002. Nanomechanics and the viscoelastic behavior of carbon nanotube-reinforced polymers. Mechanical engineering, Northwestern University, Evanston, IL.

Fisher, F. T., Bradshaw, R. D., Brinson, L. C., 2002. Effects of nanotube waviness on the modulus of nanotube-reinforced polymers. Applied Physics Letters 80 (24), 4647–4649.

Flanagan, D., 1983. Correction. International Journal for Numerical Methods in Engineering 19 (3), 467–468.

Flanagan, D., Belytschko, T., 1981. Uniform strain hexahedron and quadrilateral with orthogonal hourglass control. International Journal for Numerical Methods in Engineering 17 (5), 679–706.

Frankland, S., Caglar, A., Brenner, D., Griebel, M., November 27-30 2000. Reinforcement mechanisms in polymer nanotube composites: simulated non-bonded and cross-linked systems. In: Nanotubes and Related Materials Symposium. Vol. 633. Materials Research Society, Boston, Massachusetts, pp. A14.17.1–A14.17.5.

Frankland, S., Harik, V., Odegard, G., Brenner, D., Gates, T., 2002. The stress-strain behavior of polymer-nanotube composites from molecular dynamics simulations. Tech. rep., NASA ICASE.

Frankland, S., Harik, V., Odegard, G., Brenner, D., Gates, T., 2003. The stress-strain behavior of polymer-nanotube composites from molecular dynamics simulation. Composites Science and Technology 63, 1655–1661.

Ghosh, S., Moorthy, S., 1995. Elastic-plastic analysis of arbitrary heterogeneous materials with the voronoi cell finite element method. Computer Methods in Applied Mechanics and Engineering 121, 373–409.

Ghosh, S., Nowak, Z., Lee, K., 1997. Quantitative characterization and modeling of composite microstructures by voronoi cells. Acta Materialia 45 (6), 2215–2234.

Gong, X., Liu, J., Baskaran, S., Voise, R., Young, J., 2000. Surfactant-assisted processing of carbon nanotube/polymer composites. Chemistry of Materials 12 (4), 1049–1052.

Griebel, M., Hamaekers, J., 2004. Molecular dynamics simulations of the elastic moduli of polymer-carbon nanotube composites. Computer Methods in Applied Mechanics and Engineering 193, 1773–1788.

Hadjiev, V. G., Lagoudas, D., Oh, E.-S., Thakre, P., Davis, D., Files, B. S., Yowell, L., Arepalli, S., Bahr, J., Tour, J., 2006. Buckling instabilities of octadecylamine functionalized carbon nanotubes embedded in epoxy. Composites Science and Technology 66 (1), 128–136.

Hammerand, D., Seidel, G., Lagoudas, D., 2007. Computational micromechanics of clustering and interphase effects in carbon nanotube composites. Mechanics of Advanced Materials and Structures , Accepted; In Press.

Hashin, Z., 2002. Thin interphase/imperfect interface in elasticity with application to coated fiber composites. Journal of the Mechanics and Physics of Solids 50, 2509–2537.

Hashin, Z., Rosen, B., 1964. The elastic moduli of fiber-reinforced materials. Journal of Applied Mechanics 31, 223–232.

Hill, R., 1965. A self-consistent mechanics of composite materials. Journal of Mechanics and Physics of Solids 13, 213–222.

Iijima, S., 1991. Helical microtubules of graphitic carbon. Nature 354, 56.

in het Panhuis, M., Maiti, A., Dalton, A., van den Noort, A., Coleman, J., McCarthy, B., Blau, W., 2003. Selective interaction in a polymer-single wall carbon nanotube composite. Journal of Physical Chemistry B 107, 478–482.

Jin, L., Bower, C., Zhou, O., August 1998. Alignment of carbon nanotubes in a polymer matrix by mechanical stretching. Applied Physics Letters 73 (9), 1197–1199.

Kataoko, Y., Taya, M., 2000. Analysis of mechanical behavior of a short fiber composite using micromechanics based model (effects of fiber clustering on composite stiffness). JSME International Journal 43 (1), 46–52.

Lagoudas, D., Gavazzi, A., Nigam, H., 1991. Elastoplastic behavior of metal matrix composites based on incremental plasticity and the mori-tanaka averaging scheme. Computational Mechanics 8, 193–203.

Liu, Y., Chen, X., 2003. Evaluations of the effective material properties of carbon nanotube-based composites using nanoscale representative volume element. Mechanics of Materials 35, 69–81.

Lourie, O., Wagner, H., 1998. Transmission electron microscopy observations of fracture of single-wall carbon nanotubes under axial tension. Applied Physics Letters 73 (24), 3527–3529.

Lu, J. P., 1997. Elastic properties of single and multilayered nanotubes. Journal of Physics and Chemistry of Solids 58 (11), 1649–1652.

McCarthy, B., Coleman, J., Czerw, R., Dalton, A., in het Panhuis, M., Maiti, A., Drury, A., Bernier, P., Nagy, J., Lahr, B., Byrne, H., Carroll, D., Blau, W., 2002. A microscopic and spectroscopic study of interactions between carbon nanotubes and a conjugated polymer. Journal of Physical Chemistry B 106, 2210–2216.

Milo, S., Shaffer, P., Windle, A. H., 1999. Fabrication and characterization of carbon nanotube/poly(vinyl alcohol) composites. Advanced Materials 11 (11), 937–941.

Mori, T., Tanaka, K., 1973. Average stress in matrix and average elastic energy of materials with misfitting inclusions. Acta Metallurgica 21, 571–574.

Mori, T., Wakashima, K., Tanaka, K., 1973. Plastic deformation anisotropy and work-hardening of composite materials. Journal of Mechanics and Physics of Solids 21, 207–214.

Namilae, S., Chandra, N., Shet, C., 2004. Mechanical behavior of functionalized nanotubes. Chemical Physics Letters 387, 247–252.

Odegard, G., Clancy, T., Gates, T., 2005. Modeling of the mechanical properties of nanoparticle/polymer composites. Polymer 46, 553–562.

Odegard, G., Gates, T., June 10-12 2002. Constitutive modeling of nanotube/polymer composites with various nanotube orientatons. In: 2002 SEM Annual Conference on Experimental and Applied Mechanincs, June 10-12, 2002, Milwaukee, WI. SEM, Milwaukee, WI.

Odegard, G., Gates, T., Wise, K., 2002a. Constitutive modeling of nanotube-reinforced polymer composites. Tech. rep., AIAA.

Odegard, G., Gates, T., Wise, K., Park, C., Siochi, E., 2002b. Constitutive modeling of nanotube-reinforced polymer composites. Tech. rep., NASA ICASE.

Odegard, G., Gates, T., Wise, K., Park, C., Siochi, E., 2003. Constitutive modeling of nanotube-reinforced polymer composites. Composites Science and Technology 63, 1671–1687.

Odegard, G., Harik, V., Wise, K., Gates, T., 2001. Constitutive modeling of nanotube-reinforced polymer composite systems. Tech. rep., NASA.

Peigney, A., Laurent, C., Flahaut, E., Rousset, A., 2000. Carbon nanotubes in novel ceramic matrix nanocomposites. Ceramics International 26, 677–683.

Pierson, K., Hales, J., Alvin, K., Mitchell, J., 2005. Adagio/Andante User's Guide Version 2.0. Sandia National Laboratories, Albuquerque, N.M., 87185.

Popov, V., 2004. Carbon nanotubes: properties and applications. Materials Science and Engineering R 43, 61–102.

Potschke, P., Bhattacharyya, A., Janke, A., 2004. Carbon nanotube-filled polycarbonate composites produced by melt mixing and their use in blends with polyethylene. Carbon 42, 965–969.

Qian, D., Dickey, E., Andrews, R., Rantell, T., 2000. Load transfer and deformation mechanisms in carbon nanotube-polystyrene composites. Applied Physics Letters 76 (20), 2868–2870.

Qian, D., Liu, W. K., Ruoff, R. S., 2003. Load transfer mechanisms in carbon nanotube ropes. Composites Science and Technology 63, 1561–1569.

Qiu, Y., Weng, G., 1990. On the application of mori-tanaka's theory involving transversely isotropic spheroidal inclusions. International Journal of Engineering Science 28 (11), 1121–1137.

Roche, S., 2000. Carbon nanotubes: exceptional mechanical and electronic properties. Annales de Chemie Science des Materiaux 25, 529–532.

Ruoff, R. S., Lorents, D. C., 1995. Mechanical and thermal properties of carbon nanotubes. Carbon 33, 925–930.

Saito, R., Dresselhaus, G., Dresselhaus, M., 1998. Physical Properties of Carbon Nanotubes. Imperial College Press.

Salvetat-Delmotte, J.-P., Rubio, A., 2002. Mechanical properties of carbon nanotubes: a fiber digest for beginners. Carbon 40, 1729–1734.

Schadler, L., Giannaris, S. C., Ajayan, P. M., 1998. Load transfer in carbon nanotube epoxy composites. Applied Physics Letters 73 (26), 3842–3844.

Seidel, G., Lagoudas, D., 2006a. Micromechanical analysis of the effective elastic properties of carbon nanotube reinforced composites. Mechanics of Materials 38, 884–907.

Seidel, G., Lagoudas, D., 2006b. Micromechanical analysis of the effective elastic properties of carbon nanotube reinforced composites. Mechanics of Materials 38 (8-10).

Seidel, G., Lagoudas, D., Frankland, S., Gates, T., September 7-9 2005. Modeling functionally graded interphase regions in carbon nanotube reinforced composites. In: Proceedings of the 20th ASC Technical Conference. American Society for Composites, Drexel University, Philadelphia, PA.

Spitzag, W., Kelly, J., Richmond, O., 1985. Quantative characterization of second phase populations. Metallography 18, 235–261.

Star, A., Stoddart, J., Steuerman, D., Diehl, M., Boukai, A., Wong, E., 2001. Preparation and properties of polymer-wrapped single-walled carbon nanotubes. Angewandte Chemie International Edition 40 (9), 1721–1725.

Tszeng, T., 1998. The effects of particle clustering on the mechanical behavior of particle reinforced composites. Composites Part B: Engineering 29B, 299–308.

Wagner, H., 1996. Thermal residual stress in composites with anisotropic interphases. Physical Review B 53 (9), 5055–5058.

Wagner, H., July 2002. Nanotube-polymer adhesion: a mechanics approach. Chemical Physics Letters 361, 57–61.

Wagner, H., Lourie, O., Feldman, Y., Tenne, R., 1998. Stress-induced fragmentation of multiwall carbon nanotubes in a polymer matrix. Applied Physics Letters 72 (2), 188–190.

Wagner, H., Nairn, J., 1997. Residual thermal stresses in three concentric transversely isotropic cylinders: application to thermoplastic-matrix composites containing a transcrystalline interphase. Composites Science and Technology 57, 1289–1302.

Wang, Z. L., Gao, R. P., Poncharal, P., de Heer, W. A., Dai, Z. R., Pan, Z. W., 2001. Mechanical and electrostatic properties of carbon nanotubes and nanowires. Materials Science and Engineering C 16, 3–10.

Watts, P., Ponnampalam, D., Hsu, W., Barnes, A., Chambers, B., 2003. The complex permittivity of mulit-walled carbon nanotube-polystyrene composite films in x-band. Chemical Physics Letters 378, 609–614.

Weng, G., 1984. Some elastic properties of reinforced solids, with special reference to isotropic ones containing spherical inclusions. International Journal of Engineering Science 22, 845–856.

Wray, P., Richmond, O., Morrison, H., 1983. Use of the dirichlet tessellation for characterizing and modeling nonregular dispersions of second-phase particles. Metallography 16, 39–58.

Yakobson, B., Smalley, R., 1997. Fullerene nanotubes: C1,000,000 and beyond. American Scientist 85, review of Nanotubes.

Yakobson, B. I., Campbell, M. P., Brabec, C. J., Bernholc, J., 1997. High strain rate fracture and c-chain unraveling in carbon nanotubes. Computational Materials Science 8, 341–348.

Yang, S., Castilleja, J., Barrera, E., Lozano, K., 2004. Thermal analysis of an acrylonitrile-butadiene-styrene/swnt composite. Polymer Degradation and Stability 83, 383–388.

Yu, M.-F., Files, B. S., Arepalli, S., Ruoff, R., 2000a. Tensile loading of ropes of single wall carbon nanotubes and their mechanical properties. Physical Review Letters 84 (24), 5552–5555.

Yu, M.-F., Lourie, O., Dyer, M. J., Maloni, K., Kelly, T. F., Ruoff, R. S., 2000b. Strength and breaking mechanism of multi-walled carbon nanotubes under tensile load. Science 287 (28), 637–640.

Zhu, J., Kim, J., Peng, H., Margrave, J., Khabashesku, V., Barrera, E., 2003. Improving the dispersion and integration of single-walled carbon nanotubes in epoxy composites through functionalization. Nano Letters 3 (8), 1107–1113.

Zhu, J., Peng, H., Rodriguez-Macias, F., Margrave, J., Khabashesku, V., Imam, A., Lozano, K., Barrera, E., 2004. Reinforcing epoxy polymer composites through covalent integration of functionalized nanotubes. Advanced Functional Materials 14 (7), 643–648.

Appendix A

Summary of Composite Cylinders Micromechanics Solutions

A brief summary of the composite cylinders assemblage used for obtaining the effective properties of well-dispersed CNTs with no interphase region (Figure A.1) is discussed herein. The methodology is taken from Hashin and Rosen (1964) wherein the effective transversely isotropic properties of hollow isotropic fibers embedded in an isotropic matrix, i.e. without interphase regions, were derived for aligned fiber composites. Details of the approach as applied to the composite system studied herein to investigate clustering and interphase effects can be found in previous work by Seidel and Lagoudas Seidel and Lagoudas (2006a). It should be noted that displacement fields provided in the subsections which follow are solutions to Eqns. 3.14 through 3.16 in cylindrical coordinates. It should also be noted that in the schematic of the composite cylinder method provided in Figure A.1, the tube axis is along the one-, or z-direction. The inner radius of the fiber is denoted as r_0, and the outer radius of the matrix is denoted as r_2, with r_1 denoting the fiber outer radius. Displacements and tractions across each phase boundary are assumed to be continuous.

A.1 In-Plane Bulk Modulus

The effective in-plane bulk modulus, κ_{23}, for the composite cylinder assemblage of Figure A.1 is determined through the application of the following displacement field expressed in cylindrical coordinates:

$$\begin{aligned} u_r^{(i)} &= B_1^{(i)} r + B_2^{(i)} \frac{1}{r} \\ u_\theta^{(i)} &= 0 \qquad\qquad \text{for } r_{i-1} \leq r \leq r_i \\ u_z^{(i)} &= 0 \end{aligned} \tag{A.1}$$

where $B_1^{(i)}$ and $B_2^{(i)}$ are constants and (i) ranges from one to two. These displacements are used to calculate first the strains and then the stresses within the composite cylinder in

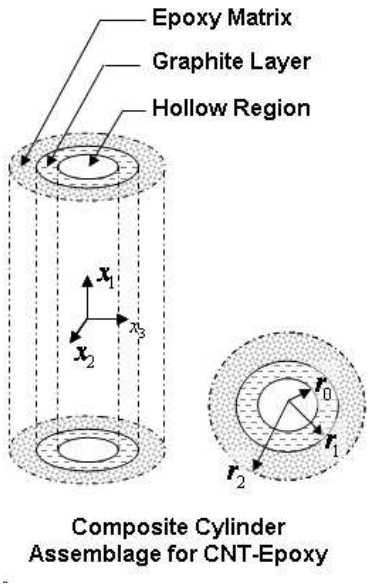

Figure A.1. Composite cylinder assemblage used in initial micromechanics evaluation of the effective properties of CNT-epoxy composites Seidel and Lagoudas (2006a).

terms of the unknown constants. The constants are determined through the application of the boundary conditions:

$$\sigma_{rr}^{(1)}|_{r=r_0} = 0 \tag{A.2}$$

$$u_r^{(2)}|_{r=r_2} = \varepsilon_0 r_2 \tag{A.3}$$

where ε_0 is the radial strain applied at the boundary. The two additional equations needed to determine the unknown constants are found in the continuity of displacement and traction conditions given by:

$$u_r^{(1)}|_{r=r_1} = u_r^{(2)}|_{r=r_1} \tag{A.4}$$

$$\sigma_{rr}^{(1)}|_{r=r_1} = \sigma_{rr}^{(2)}|_{r=r_1} \tag{A.5}$$

The constants in the displacement field are then determined to be:

$$
\begin{aligned}
B_2^{(2)} &= \frac{\varepsilon_0}{\left[\frac{1}{r_2^2} - \frac{1}{r_1^2}\left(\frac{\alpha_1\alpha_2 + G_2}{\alpha_1\alpha_2 - (G_2+\lambda_2)}\right)\right]} \\
B_1^{(2)} &= \left(\frac{-(\alpha_1\alpha_2 + G_2)}{r_1^2[\alpha_1\alpha_2 - (G_2+\lambda_2)]}\right) B_2^{(2)} \\
B_2^{(1)} &= \frac{\alpha_1}{G_1}\left(B_1^{(2)} + \frac{1}{r_1^2}B_2^{(2)}\right) \\
B_1^{(1)} &= \left(\frac{G_1}{r_0^2(G_1+\lambda_1)}\right) B_2^{(1)}
\end{aligned}
\tag{A.6}
$$

where G_1 and λ_1 are the Lamé constants of the graphite layer, G_2 and λ_2 are the Lamé constants of the epoxy, and α_1 and α_2 are given by:

$$
\begin{aligned}
\alpha_1 &= \frac{G_1}{\left[\left(\frac{G_1}{G_1+\lambda_1}\right)\frac{1}{r_0^2} + \frac{1}{r_1^2}\right]} \\
\alpha_2 &= \left(\frac{1}{r_0^2} - \frac{1}{r_1^2}\right)
\end{aligned}
\tag{A.7}
$$

The effective in-plane bulk modulus, κ_{23} is then obtained by:

$$
\kappa_{23} = \frac{\langle \sigma_{rr} \rangle}{2\langle \varepsilon_{rr} \rangle} \tag{A.8}
$$

where $\langle \bullet \rangle$ denotes a volume average as defined by:

$$
\langle \bullet \rangle = \frac{1}{V}\int_V \bullet \, dV \tag{A.9}
$$

It can be shown that Eqn. A.8 can be expressed in terms of the stress and displacement at the boundary of the composite cylinder assemblage as:

$$
\kappa_{23} = \frac{\sigma_{rr}^{(2)}|_{r=r_2}}{2\left(u_r^{(2)}|_{r=r_2}/r_2\right)} \tag{A.10}
$$

A.2 Axial Modulus E_{11} and ν_{12} Poisson's Ratio

The effective axial modulus, E_{11}, and ν_{12} Poisson's ratio for the composite cylinder assemblage of Figure A.1 is determined through the application of the following displacement

field expressed in cylindrical coordinates:

$$\begin{aligned} u_r^{(i)} &= B_1^{(i)} r + B_2^{(i)} \frac{1}{r} \\ u_\theta^{(i)} &= 0 \qquad\qquad \text{for } r_{i-1} \leq r \leq r_i \\ u_z^{(i)} &= \varepsilon_0 z \end{aligned} \tag{A.11}$$

where $B_1^{(i)}$ and $B_2^{(i)}$ are again constants, ε_0 is the applied uniaxial strain, and (i) ranges from one to two. These displacements are used to calculate first the strains and then the stresses within the composite cylinder. The constants are determined through the application of the following boundary conditions:

$$\sigma_{rr}^{(1)}|_{r=r_0} = 0 \tag{A.12}$$

$$\sigma_{rr}^{(2)}|_{r=r_2} = 0 \tag{A.13}$$

and continuity of displacement and traction conditions given by:

$$u_r^{(1)}|_{r=r_1} = u_r^{(2)}|_{r=r_1} \tag{A.14}$$

$$\sigma_{rr}^{(1)}|_{r=r_1} = \sigma_{rr}^{(2)}|_{r=r_1} \tag{A.15}$$

The constants in the displacement field are determined to be:

$$\begin{aligned} B_2^{(2)} &= \frac{\beta_3}{\alpha_6}\varepsilon_0 \\ B_1^{(2)} &= \frac{\beta_2}{\alpha_4}\varepsilon_0 + \frac{\alpha_5}{\alpha_4}\frac{1}{r_1^2}B_2^{(2)} \\ B_2^{(1)} &= \alpha_2\left(\beta_1\varepsilon_0 + B_1^{(2)} + \frac{1}{r_1^2}B_2^{(2)}\right) \\ B_1^{(1)} &= \alpha_1\frac{1}{r_0^2}B_2^{(1)} - \beta_1\varepsilon_0 \end{aligned} \tag{A.16}$$

where the α_i are given by:

$$\begin{aligned}
\alpha_1 &= \frac{G_1}{G_1+\lambda_1} \\
\alpha_2 &= \frac{1}{\left(\alpha_1\frac{1}{r_0^2}+\frac{1}{r_1^2}\right)} \\
\alpha_3 &= 2\left(G_1+\lambda_1\right)\alpha_1\frac{1}{r_0^2}-2G_1\frac{1}{r_1^2} \\
\alpha_4 &= \alpha_2\alpha_3-2(G_2+\lambda_2) \\
\alpha_5 &= -\alpha_2\alpha_3-2G_2 \\
\alpha_6 &= 2(G_2+\lambda_2)\frac{\alpha_5}{\alpha_4}\frac{1}{r_1^2}-2G_2\frac{1}{r_2^2}
\end{aligned} \tag{A.17}$$

and where the β_i are given by:

$$\begin{aligned}
\beta_1 &= \frac{\lambda_1}{2(G_1+\lambda_1)} \\
\beta_2 &= \lambda_2-\lambda_1+\beta_1[2(G_2+\lambda_2)-\alpha_2] \\
\beta_3 &= -\lambda_2-2(G_2+\lambda_2)\frac{\beta_2}{\alpha_4}
\end{aligned} \tag{A.18}$$

The effective axial modulus, E_{11}, is then obtained by:

$$E_{11} = \frac{\langle\sigma_{zz}\rangle}{\langle\varepsilon_{zz}\rangle} \tag{A.19}$$

where the volume averaged stress, $\langle\sigma_{zz}\rangle$, is given by:

$$\langle\sigma_{zz}\rangle = \frac{2\pi L}{\pi L r_2^2}\left[\sum_{i=1}^{2}\int_{r_{i-1}}^{r_i}\sigma_{zz}^{(i)} r\,dr\right] \tag{A.20}$$

where L is the arbitrary length of the composite cylinder assemblage and where it is noted that there is zero stress in the hollow region of the fiber. The volume averaged strain is similarly calculated as:

$$\langle\varepsilon_{zz}\rangle = \frac{2\pi L}{\pi L r_2^2}\left[\varepsilon_0\frac{r_0^2}{2}+\sum_{i=1}^{2}\int_{r_{i-1}}^{r_i}\varepsilon_{zz}^{(i)} r\,dr\right] \tag{A.21}$$

where the additional term before the sum acknowledges the non-zero strains in the hollow of the fiber so that $\langle\varepsilon_{zz}\rangle = \varepsilon_0$ is maintained.

From the same applied strain, the effective ν_{12} Poisson's ratio of the composite cylinder assemblage is obtained as indicated by Christensen (1979) from:

$$\nu_{12} = \frac{-\langle \varepsilon_{rr} \rangle}{\langle \varepsilon_{zz} \rangle} \tag{A.22}$$

so that

$$\nu_{12} = \frac{-\left(u_r^{(2)}|_{r=r_2}/r_2\right)}{\varepsilon_0} \tag{A.23}$$

A.3 G_{12} Shear Modulus

For determining the effective G_{12} shear modulus of the composite cylinder assemblage use of the energy equivalence between the composite cylinder assemblage and a homogeneous solid effective cylinder will be used. The following displacement field, expressed in cylindrical coordinates, is applied to the composite cylinder arrangement:

$$\begin{aligned} u_r^{(i)} &= 0 \\ u_\theta^{(i)} &= 0 \qquad\qquad \text{for } r_{i-1} \leq r \leq r_i \\ u_z^{(i)} &= \left(B_1^{(i)} r + B_2^{(i)} \frac{1}{r}\right) \cos(\theta) \end{aligned} \tag{A.24}$$

where $B_1^{(i)}$ and $B_2^{(i)}$ are again constants and (i) ranges from one to two. These displacements are used to calculate first the strains and then the stresses within the composite cylinder. The constants are determined through the application of the following boundary conditions:

$$G_1 \frac{\partial u_z^{(1)}}{\partial r}|_{r=r_0} = 0 \tag{A.25}$$

$$u_r^{(2)}|_{r=r_2} = 2\varepsilon_0 r_2 \cos(\theta) \tag{A.26}$$

where G_1 is the shear modulus of the graphite and ε_0 is the shear strain applied at the boundary. The continuity of displacement and traction conditions are given by:

$$u_z^{(1)}|_{r=r_1} = u_z^{(2)}|_{r=r_1} \tag{A.27}$$

$$G_1 \frac{\partial u_z^{(1)}}{\partial r}|_{r=r_1} = G_2 \frac{\partial u_z^{(2)}}{\partial r}|_{r=r_1} \tag{A.28}$$

The constants in the displacement field are then determined to be:

$$\begin{aligned} B_2^{(2)} &= \frac{2\varepsilon_0}{\left(\frac{\alpha_4}{\alpha_3}\frac{1}{r_1^2}+\frac{1}{r_2^2}\right)} \\ B_1^{(2)} &= \frac{\alpha_4}{\alpha_3}\frac{1}{r_1^2}B_2^{(2)} \\ B_2^{(1)} &= \frac{1}{\alpha_1}\left(B_1^{(2)}+\frac{1}{r_1^2}B_2^{(2)}\right) \\ B_1^{(1)} &= \frac{1}{r_0^2}B_2^{(1)} \end{aligned} \tag{A.29}$$

where the α_i are given by:

$$\begin{aligned} \alpha_1 &= \left(\frac{1}{r_0^2}+\frac{1}{r_1^2}\right) \\ \alpha_2 &= \left(\frac{1}{r_0^2}-\frac{1}{r_1^2}\right) \\ \alpha_3 &= \left(\frac{\alpha_2}{\alpha_1}-\frac{G_2}{G_1}\right) \\ \alpha_4 &= \left(-\frac{\alpha_2}{\alpha_1}-\frac{G_2}{G_1}\right) \end{aligned} \tag{A.30}$$

Solving the same boundary value problem, but for the effective solid homogeneous material, the displacement field in the effective solid is then given by:

$$\begin{aligned} u_r^{(*)} &= 0 \\ u_\theta^{(*)} &= 0 \qquad\qquad \text{for } 0 \le r \le r_2 \\ u_z^{(*)} &= 2\varepsilon_0 r\cos(\theta) \end{aligned} \tag{A.31}$$

where the superscript $(*)$ denotes the effective homogeneous solid. The effective G_{12} shear modulus of the composite cylinder assemblage is then obtained by equating the strain energies of the composite cylinder to the effective homogeneous solid which, noting that both representations are subject to the same strain, can be expressed as:

$$G_2\frac{\partial u_z^{(2)}}{\partial r}|_{r=r_2} = G_{12}\frac{\partial u_z^{(*)}}{\partial r}|_{r=r_2} \tag{A.32}$$

and solving for G_{12}.

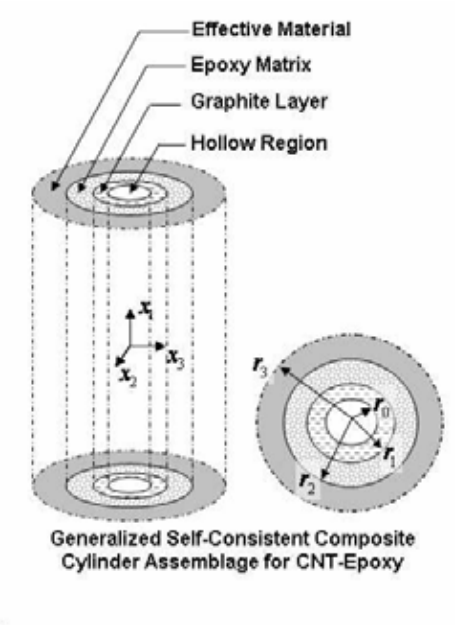

Figure A.2. Generalized self-consistent composite cylinder assemblage used in initial micromechanics evaluation of the effective properties of CNT-epoxy composites Seidel and Lagoudas (2006b).

A.4 G_{23} Shear Modulus

In determining the effective G_{23} shear modulus of the composite cylinder assemblage, the entire assemblage is embedded in a layer whose material properties are the same as the material properties of the effective solid homogeneous material as shown in Figure A.2. This modified composite cylinders assemblage was first proposed by Christensen and Lo (1979) and is referred to as the generalized self-consistent technique. The effective G_{23} shear modulus of the composite cylinder assemblage is determined through the use of the energy equivalence between the generalized self-consistent composite cylinder assemblage and a homogeneous solid effective cylinder. The following displacement field, expressed in cylindrical coordinates, is applied to the composite cylinder arrangement:

$$\begin{aligned} u_r^{(i)} &= \left(B_1^{(i)} r + \left(\frac{\lambda_i}{3G_i + 2\lambda_i} \right) B_2^{(i)} r^3 - B_3^{(i)} r^{-3} + \left(\frac{2G_i + \lambda_i}{G_i} \right) B_4^{(i)} r^{-1} \right) \sin(2\theta) \\ u_\theta^{(i)} &= \left(B_1^{(i)} r + B_2^{(i)} r^3 + B_3^{(i)} r^{-3} + B_4^{(i)} r^{-1} \right) \cos(2\theta) \qquad \text{for } r_{i-1} \leq r \leq r_i \\ u_z^{(i)} &= 0 \end{aligned} \tag{A.33}$$

where i ranges from one to two and where the $B_k^{(i)}$ (k=1,..,4 and i=1,..,2) are constants to be determined and G_i and λ_i are the Lamé constants for the i^{th} phase. For the displacement field in the surrounding effective material, i.e. the 3^{rd} phase, Christensen (1979) has provided a convenient expression of the displacement field where the boundary conditions on the external surface have been applied as:

$$\begin{aligned} u_r^{(3)} &= \left(\frac{r_3}{4G_{23}}\right)\left(\frac{2}{r_3}r + (4-4\nu_{23})r_3 D_5 r^{-1} + r_3^3 D_6 r^{-3}\right)\sin(2\theta) \\ u_\theta^{(3)} &= \left(\frac{-r_3}{4G_{23}}\right)\left(-\frac{2}{r_3}r + (-2+4\nu_{23})r_3 D_5 r^{-1} + r_3^3 D_6 r^{-3}\right)\cos(2\theta) \qquad \text{for } r_2 \le r \le r_3 \\ u_z^{(3)} &= 0 \end{aligned} \tag{A.34}$$

where D_5 and D_6 are constants, G_{23} and ν_{23} are the effective in-plane shear modulus and Poisson's ratio, respectively, of the composite cylinder assemblage, and r_3 is the outer radius of the 3^{rd} phase which is arbitrary and can be taken to infinity. These displacements are used to calculate first the strains and then the stresses within the composite cylinder subject to the boundary conditions on the inner surface of:

$$\sigma_{rr}^{(1)}|_{r=r_0} = 0 \tag{A.35}$$

$$\sigma_{r\theta}^{(1)}|_{r=r_0} = 0 \tag{A.36}$$

and continuity of displacement and traction conditions given by:

$$u_r^{(j)}|_{r=r_j} = u_r^{(j+1)}|_{r=r_j} \tag{A.37}$$

$$u_\theta^{(j)}|_{r=r_j} = u_\theta^{(j+1)}|_{r=r_j} \tag{A.38}$$

$$\sigma_{rr}^{(j)}|_{r=r_j} = \sigma_{rr}^{(j+1)}|_{r=r_j} \tag{A.39}$$

$$\sigma_{r\theta}^{(j)}|_{r=r_j} = \sigma_{r\theta}^{(j+1)}|_{r=r_j} \tag{A.40}$$

where j ranges from one to two. One can then obtain the six unknown constants, B_k^i, D_5, and D_6, by solving the system of algebraic equations in Eqns. A.35 through A.40.

The displacement field for the effective homogeneous solid material, is given by:

$$\begin{aligned} u_r^{(*)} &= \left(\frac{r_3}{4G_{23}}\right)\left(\frac{2}{r_3}r\right)\sin(2\theta) \\ u_\theta^{(*)} &= \left(\frac{-r_3}{4G_{23}}\right)\left(-\frac{2}{r_3}r\right)\cos(2\theta) \qquad \text{for } 0 \le r \le r_3 \\ u_z^{(*)} &= 0 \end{aligned} \tag{A.41}$$

where there are no constant terms like those in Eqn. A.34 as a result of the requirement that the displacement field be bounded at the origin. It is then observed that equivalence of strain energies of the effective homogeneous solid with the composite cylinder assemblage using the Eshelby formula can be expressed as:

$$\int_0^{2\pi} \left[\sigma_{rr}^{(3)} u_r^{(*)} + \sigma_{r\theta}^{(3)} u_\theta^{(*)} - \left(\sigma_{rr}^{(*)} u_r^{(3)} + \sigma_{r\theta}^{(*)} u_\theta^{(3)} \right) \right]_{r=r_2} d\theta = 0 \tag{A.42}$$

which to be satisfied, indicates that D_5 in Eqn. A.34, which, as a result of solving the system of Eqns. A.35 through A.40, is in terms of G_1, λ_1, G_2, λ_2, r_0, r_1, r_2, and G_{23}, should be identically zero. Thus, G_{23} is then obtained by setting:

$$D_5 = 0 \tag{A.43}$$

and solving for G_{23}. It should be noted that the algebra involved in obtaining D_5, and indeed the other constants in the composite cylinders assemblage, in terms of the unknown effective properties is quite intensive and as such, Cramer's rule has been used to solve only for the needed expression of D_5.

A.5 Transverse Modulus E_{22} and ν_{23} Poisson's Ratio

Finally, the transverse modulus for the composite cylinders assemblage is calculated in terms of the in-plane bulk modulus, axial modulus, ν_{12} Poisson's ratio, and G_{23} shear modulus as:

$$E_{22} = \frac{4 G_{23} \kappa_{23}}{\kappa_{23} + G_{23} + 4 \nu_{12}^2 G_{23} \kappa_{23} / E_{11}} \tag{A.44}$$

and the ν_{23} Poisson's ratio is obtained as:

$$\nu_{23} = \frac{\kappa_{23} - G_{23} - 4 \nu_{12}^2 G_{23} \kappa_{23} / E_{11}}{\kappa_{23} + G_{23} + 4 \nu_{12}^2 G_{23} \kappa_{23} / E_{11}} \tag{A.45}$$

DISTRIBUTION:

1 Dimitris C. Lagoudas
Department of Aerospace Engineering
Texas A&M University
College Station, Texas 77843-3141

1 Gary D. Seidel
Department of Aerospace Engineering
Texas A&M University
College Station, Texas 77843-3141

3 Dwight Look College of Engineering
Texas A&M University
College Station, Texas 77843-3126

3	MS 0372	D.C. Hammerand, 01524
1	MS 0372	J. Pott, 01524
1	MS 0372	J.M. Redmond, 01525
1	MS 0372	File Copy, 01524
1	MS 0372	L. Worrel, 01524
1	MS 0555	R.A. May, 01522
1	MS 0557	D.B. Clauss, 01521
1	MS 0826	C.C. Wong, 01526
1	MS 0847	T.J. Baca, 01523
1	MS 0847	P.J. Wilson, 01520
1	MS 0888	R.S. Chambers, 01524
1	MS 0888	E.D. Reedy, 01526
1	MS 9042	J.W. Foulk, 08776
1	MS 9042	E.P. Chen, 08776
2	MS 9018	Central Technical Files, 8944
2	MS 0899	Technical Library, 4536
1	MS 0123	D. Chavez, LDRD Office, 1011